Rafael Schio Wengenroth Silva

The Memristive Response in Solids

São Carlos

August 07, 2023

Rafael Schio Wengenroth Silva

The Memristive Response in Solids

Master's thesis submitted to the Graduate Program of Physics at the Federal University of São Carlos, in partial fulfillment of the requirements for obtaining the degree of Master of Science in Physics.

Federal University of São Carlos – UFSCar

Center of Exact Sciences and Technology

Graduate Program of Physics

Supervisor: Prof. Dr. Victor Lopez-Richard

São Carlos

August 07, 2023

Rafael Schio Wengenroth Silva

The Memristive Response in Solids

Master's thesis submitted to the Graduate Program of Physics at the Federal University of São Carlos, in partial fulfillment of the requirements for obtaining the degree of Master of Science in Physics.

Graduate Advisory Committee:

Prof. Dr. Victor Lopez-Richard
Supervisor

Professor
Committee Member 1

Professor
Committee Member 2

Professor
Committee Member 3

Professor
Committee Member 4

Date defended/Approved: August 07, 2023

São Carlos
August 07, 2023

To my family and my fiancée.

Acknowledgements

I am deeply grateful to my advisor, Professor Victor Lopez-Richard, for his unwavering support and guidance throughout my master's program. His expertise and patience have been invaluable to me and have played a crucial role in the success of this thesis. Due to him, I had the opportunity to do real research for the first time in my life, being this experience an essential contribution to my current stage as a researcher. His attitudes will remain with me as memories of what a good researcher and person should be. Thank you by being always present to guide me through my way. And thank you for pushing me harder in the activities: this attitude motivated me to follow your steps, trying to keep close of your highly productivity research standards, what certainly sharpened my research skills; and also, I am grateful for being kind and helpful when hard times occurred to me. More than that, Professor Victor provided me contact with different research groups in Brazil, Germany, and USA, which was a very exciting and inspirational experience for me, at the same time that with this contact I learned how to work with different groups and the crucial importance of the experimental and theoretical efforts to interplay with each other. The acknowledgments to you, Professor, are numerous and do not end here, so one more time, I express my sincere gratitude to you: For all.

I would like to express my gratitude to Professor Ovidiu Lipan, of the University of Richmond and Fabian Hartmann, at the University of Wüzburg. Their willingness to share their experiences and insights has been invaluable to my research and has helped to make it a success. I wish to thank Professor Ovidiu for the time spent in Brazil and the work that we did together under his guidance, which was a really very exciting and meaningful experience for me; I admire the original and formal way you do physics, I have been paying attention to it and I have certainly learned something about that; I thank you also by our conversations and advises about the professional career of a researcher. To Fabian, I express my sincere gratitude for being working with us since the beginning, as Ovidiu did, and for inspiring me and for instigating my curiosity in physics. Your expertise in the *memdevices* field was fundamental for this thesis to become a reality; your insights were very intelligent and inspirational; and I also thank you by the time you spent in Brazil, for being a very kind person and for talking with me in German and answering the uncountable questions that I unavoidably had due to my curiosity.

I would like to thank Edgar David Guarin Castro, ex-PhD student of my advisor, for his help with numerous tasks, such as guiding me through the learning process of new programming languages and applying them to topics related to this research, namely, transport in semiconductors. And more than that, for being my friend and for his priceless guidance, conversations and help about many challenges that were present.

I would also like to thank my fiancée and family for their love and support during this process. Without them, this journey would not have been possible.

Finally, I am grateful to UFSCar and their Graduate Program in Physics (PPGF) for providing me with the opportunity to conduct my research and for all of the resources and support they provided. I would like to extend special thanks to CNPq, that provided me a master's scholarship that was crucial for allowing to focus all my efforts on the research.

Abstract

In this Master Thesis, we have investigated basic ingredients of the theory of solid state transport, namely the Drude like conductivity and the activation of nonequilibrium charge carriers subjected to a relaxation time, concluding that they are sufficient conditions for a memristive response. These findings point to the natural emergence of memory that, if discernible under adequate set of driving inputs, turns to be the rule and not the exception, with contrasting signatures according to symmetry constraints, either built-in or induced by external factors. Explicit analytical expressions for conductance and content are presented, unveiling very concise and accessible correlations between general intrinsic microscopic parameters such as relaxation times, activation energies, and efficiencies (encountered throughout various fields in Physics) with external drives: voltage pulses, temperature, illumination, etc. Four *toy models* under different applied bias: sinusoidal and triangular, have been investigated, providing insights about the memory formation, as well as the expressions mentioned above. The model has also been successfully applied to predict and explain memory features in samples based on ZnO thin films that were fabricated and characterized by colleagues, reinforcing its validity. The theory allowed providing values for the system's fundamental parameters, such as its relaxation time. Finally, the perspectives and directions of the forthcoming research tasks, to be continued on a PhD, are presented, pointing to the extension of the theoretical results by introducing asymmetries in the model and by exploring the topology of the current-voltage characteristics. The model can be extended to other physical systems, such as those based on quantum dots, and by applying the robust mechanism thus far constructed to study, explain, and predict results in experimental realizations, such as in oxide thin films.

Key-words: Memdevices, memory, memristors, non-equilibrium carriers.

List of Figures

Figure 1 – (a) Symbol used to represent a memristor. (b) Schematics of the transport of carriers thought several sites that are modelled with energy barriers between them within a conductor. (c) Representation of a Type-I system and its signatures: a crossing in current-voltage characteristics at zero voltage, and the corresponding double values of conductance at this point. (d) Representation of a Type-II system and its signatures: the non-crossing current-voltage characteristics and the single conductance value at zero bias voltage. 16

Figure 2 – Schematic representation of carriers activation over a barrier. The left panel represents a one dimensional energy barrier, E_B. The *quasi Fermi level* of the reservoir, located at the left side of the barrier, is represented by μ. The activated carriers pass over the barrier contributing to the one dimensional flux F_z. The right panel is a representation to reinforce that the net flux is calculated along direction z within the spherical coordinate system used in the model. 23

Figure 3 – Schematic representation of a energy barrier. At the left and right side of it, it is depicted the chemical potentials μ_L and μ_R, respectively. The energy barrier E_B separates these two regions, with the chemical potential on the right side given by $\mu_R = U + \mu_L$ and $U = -|e|V$. F_L represents the carriers flux that goes from the left reservoir to the right one over the barrier; in an analogous way, F_R represents the carrier flux from the right to the left side. In case we are dealing with electrons, due to its negative charge, if one wants to write their current densities, they will be represented with a inversion in the direction of their respective fluxes. 26

Figure 4 – (a) Schematic diagram representing the activation of trapped non-equilibrium carriers under external voltage and the local bias determined by the efficiency η, that is related with the density of generation sites in the material, namely: $\eta = Site\ Length/Total\ length$ (b) Diagram representing trapping site with metal-semiconductor-metal profile and the mechanism of promoting carriers to the conduction band by thermal excitation. 28

Figure 5 – Response difference between Type I (black lines) and Type II (red lines): (a) Transient towards the steady dynamics of nonequilibrium charge carriers under an AC voltage. (b) Current as a function of time for type I and II systems, in steady state regime. Here, N_∞ represents a sufficiently high number of periods for stability to be achieved. A solid pattern of a period of the voltage sweeps has been added in the background. (c) Type I current voltage characteristics after stability. The conductance values, G^I_{Low} and G^I_{High}, at zero bias are indicated by dashed lines while S_u and S_l label the areas of the upper and lower $I-V$ loops, respectively. (d) Type II current voltage characteristics after stability with a single conductance value, G^{II}_0, at zero bias indicated by a dashed line. (e) Stable $I-V$ response under an adiabatic voltage supply for type I and II systems. (f) Stable $I-V$ response under fast voltage oscillations for Type I and II systems. 32

Figure 6 – (a) Conductance as a function of voltage, after reaching stability. (b) Conductance at zero voltage as a function of normalized angular frequency of the applied voltage within the linear approximation, under stable cycles, for the high (on) and low (off) conductance states of Type-I systems, represented in black; and for Type-II systems, in red. (c) Calculated current-voltage loop areas for both types of systems and (on the inset) expected evolution of the loop area (in absolute arbitrary units - valid for Type-I and Type-II) with increasing temperature. . . . 33

Figure 7 – This figure shows the normalized conductance as a function of $\omega\tau$, for the first two images. The black color is used to represent the Type-I system, while the red one, the Type-II. Points are used to indicate the analytical results from the linear approximation and the lines were obtained by means of numerical calculations. In the third picture the normalized difference is depicted between the states *High* and *Low* conductance of the Type-I system, for different values of η. Note also that for $\eta = 0.01$ (continuous representation) and $\eta = 0.001$ (dashed representation) the curves almost coincide. 35

Figure 8 – In the upper image the upper and lower current-voltage areas of Type-I system are depicted for several values of η, that are represented by lines, while the dots represent the values obtained from the linear analytical approximation. In a similar way, the lower picture shows the results for the Type-II symmetrical system. While, in the inset, the expected evolution of the loop area is represented (in absolute arbitrary units valid for Types-I and II) with increasing temperature. This Figure were edited from [1]. 36

Figure 9 – Voltage $V_{Triangular}$ with a period $T = 10\,\tau$. 37
Figure 10 – Voltage V_{Tri}^{II} normalized, with a period $T = 10\,\tau$ in dark cyan, while the corresponding $V_{Triangular}$ normalized is shaded represented in cyan color. 38
Figure 11 – Transient behaviour of δn^I and δn^{II}. Parameters are: $\sigma_1 = \sigma_2 = 100;\ \tau = 1;\ T = 10;\ V_0 = 1; n_0 = 0;\ G_0 = 1;\ \alpha = 0.01$. After a sufficiently long time the systems reach the stable regimes. 45
Figure 12 – Normalized currents and voltage for one stable cycle. Parameters are: $\sigma_1 = \sigma_2 = 100;\ \tau = 1;\ T = 10;\ V_0 = 1; n_0 = 200;\ G_0 = 1;\ \alpha = 0.01$. . . 46
Figure 13 – Current voltage curves for a) Type I system, with maximum in $T = 6.75\,\tau$; and type II, with maximum in $T = 12.85\,\tau$, b).Parameters are: $\sigma_1 = \sigma_2 = 100;\ \tau = 1;\ V_0 = 1; n_0 = 200;\ G_0 = 1;\ \alpha = 0.01$. 46
Figure 14 – Normalized conductance as a function of voltage for a stable cycle. The Type-I system presents two conductance states at zero voltage, high and low, while Type-II, the symmetric one, present only one state. The parameters used are: $\sigma_1 = \sigma_2 = 100;\ \tau = 1;\ V_0 = 1; n_0 = 100;\ G_0 = 1;\ \alpha = 0.001$ and $T = 2\pi$. 47
Figure 15 – Normalized difference of the zero-conductance states with their unperturbed conductance (G_0) as functions of the period (T). The two different conductances states of Type-I system are depicted in black: the dotted line for the higher state and continuous one, for the lower. Also, the maximum difference between these states is achieved at the period $T \approx 6.022\,\tau$ (obtained numerically). The unique conduction state of the Type-II system is depicted in the red continuous line and their asymptotic values are in perfect agreement with the equations 3.70 and 3.71. Parameters are: $\sigma_1 = \sigma_2 = 100;\ \tau = 1;\ V_0 = 1; n_0 = 100;\ G_0 = 1;\ \alpha = 0.001$. 48
Figure 16 – Normalized content values for the upper loops of Type-I and (II) systems. The Type-I, black curve, presents a higher absolute value of content with a maximum at $T \approx 6.75\,\tau$; while the Type-II system, in red, presents its maximum at $T \approx 12.85\,\tau$. Parameters are: $\sigma_1 = \sigma_2 = 100;\ \tau = 1;\ V_0 = 1; n_0 = 100;\ G_0 = 1;\ \alpha = 0.001$. 49
Figure 17 – (a) Schematic representation of the sample with contacts. (b) Measured current-voltage loop with the corresponding triangular voltage drive plotted in the inset. (c) Charge density as a function of temperature. (d) Applied longitudinal voltage for each temperature to set the fixed current condition. 53

Figure 18 – (a) Measured total area of the current-voltage loop as a function of period. (b) Calculated total area of the current-voltage loop as a function of period for a triangular and a sinusoidal pulses. (c) Resistance at V = 0 as function of temperature. (d) Upper and lower loops areas as function of temperature. 54

List of Tables

Table 1 – Tuning values of period in units of τ in order to maximze the memory response of the *toy models*, regarding the content and the displacement between *High* and *Low* conductivit states of Type-I systems. 50

List of abbreviations and acronyms

f_{MB}	Maxwell-Boltzmann distribution function
$f_{FD}(E, \mu)$	Fermi-Dirac function of the energy (E) and chemical potential (μ)
D(E)	Three dimensional density of states, as a function of energy
$g(V)$	Generation Function, as a function of voltage (V)

List of symbols

m	Mass
m^*	Effective Mass
ϱ	Resistivity
k_B	Boltzmann Constant
T_{eff}	Temperature *(- effective temperature)*
T	Period
Ω	3-D volumetric region
ρ	Density of carriers
$\delta\rho$	Density of *non-equilibrium* carriers
n	Number of carriers
δn	Number of *non-equilibrium* carriers
G_0	Unperturbed conductance
α	Weight of *non-equilibrium carries* for the conductance
τ	Relaxation time
G	Conductance
I	Current
i_0	Activation coefficient over an effective energy barrier

Contents

1 INTRODUCTION . . . 15
1.1 Motivation . . . 16
1.2 Goals and Methods . . . 18
1.3 Thesis Overview . . . 19

2 THEORETICAL BACKGROUND . . . 21
2.1 Drude's Theory and Current Density . . . 21
2.1.1 Density of non-equilibrium carriers . . . 22
2.2 The model used to study the memory emergence . . . 27

3 THEORETICAL RESULTS . . . 30
3.1 Sinusoidal input . . . 30
3.1.1 Analytical Result Accuracy Beyond its Validity Regime . . . 34
3.2 Triangular input . . . 36
3.2.1 Type-I System . . . 38
3.2.2 Type-II System . . . 41
3.2.2.1 Comparing the Triangular Systems's Responses . . . 45
3.3 Optimizing the Systems . . . 50

4 EXPERIMENTAL CONFIRMATIONS AND THE EFFECT OF TEMPERATURE IN ZNO THIN FILMS . . . 51
4.1 The Model for Metal-Semiconductor-Metal Sites . . . 51
4.2 The experiment . . . 52

5 CONCLUSION AND NEXT STEPS . . . 56
5.1 Next steps . . . 57

BIBLIOGRAPHY . . . 59

1 Introduction

Memcomputing is a computational paradigm that combines information processing and storage on the same physical platform. Key elements for this topic are devices with inherent memory, namely: memristors, memconductors, and meminductors. The existence of memristors was first proposed by L. Chua [2], in 1971, as a entirely new class of electronic devices that should behave like non-linear resistors with memory. Subsequently, the idea was generalized leading to the concept of *Memristive Systems* [3], as shown in Fig. 1 (a). The most striking signature of their transport response is a *pinched hysteresis loop* in the current-voltage plane and promising applications have appeared ever since in a wide range of technological fields. The applications vary from emulation of learning rules of neural networks [4], parallel processing [5, 6], and various computing schemes [7–9]. Concerning the industrial interest in this technology, it can be pointed that in 2021 the memristive memories are being used as standalone memory and are also embedded in application-specific integrated circuits for the Internet of Things and their market value exceeded $621 million. It is also expected a growth in this market up to $5.6 billion by 2026, which will represent 2% of the nearly $280 billion memory market [10]. Besides the interest in potential applications, the memristive response might become a platform for the characterization of transport mechanisms in solids and nanoscopic systems.

Memristors have emerged in various physical platforms, such as semiconductor nanowires [11], organic materials [12], and oxides [13] producing non-volatile [12], volatile responses [14,15], semi-non-volatile responses [16], or combined dynamics [17]. A variety of models for their emulation can also be found in the literature [18] ranging from phenomenological simulations [19,20], electro-mechanical analogs [21,22], or purely mathematical protocols [23]. Yet, such a diverse range of approaches hampers a clear view of common grounds for something seemingly so pervasive in conductive solids. On these same grounds, the eventual contrast between memristive responses should be sustained as, for instance, the self-crossing [24] or not of the pinched hysteresis [25], relevant from the practical perspective and fundamental from the role played by symmetry constraints.

There are several underlying physical mechanisms of memory formation. Our efforts are focused on understanding the apparently ubiquitous memory formation mechanism in conductive solids [1] ascribed to the dynamics of nonequilibrium charge carriers, as represented in Fig. 1 (b), eventually trapped at interfaces, impurities, and defects. It is important to emphasize that memristive responses depend not only on the *generalized response functions*, that are governed by the underlying physics of each device, but also on the shape of the driving voltage pulses [18]. Furthermore, *time scales* play a role for the emergence of memory so that the voltage pulse frequency can be tuned in order to

maximize or destroy its effects.

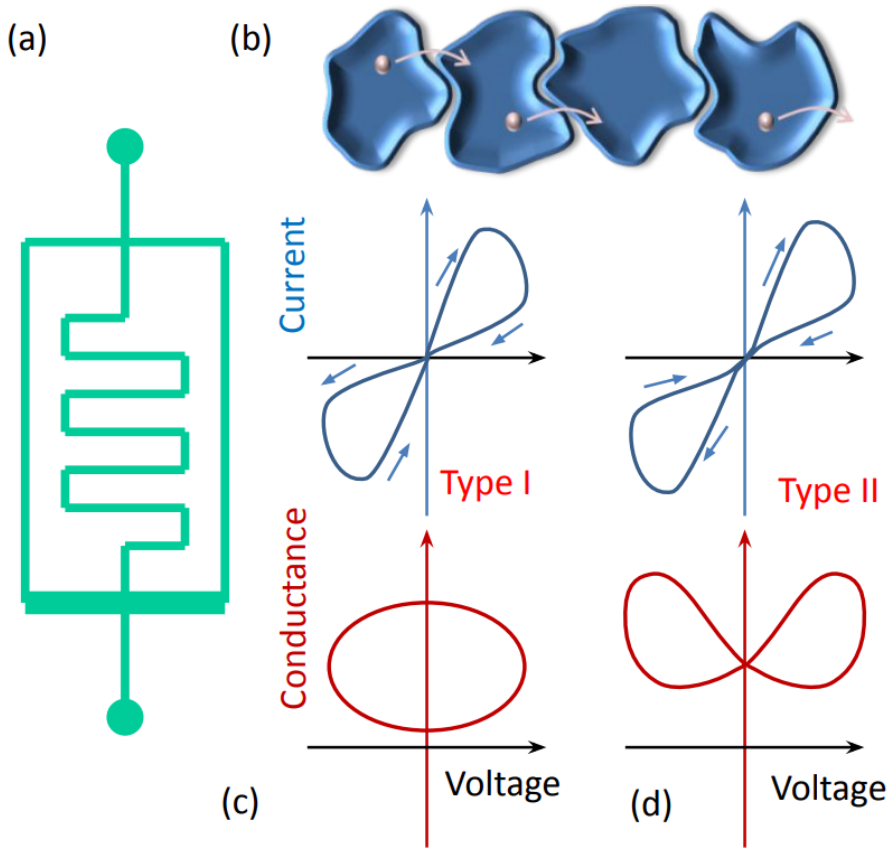

Figure 1 – (a) Symbol used to represent a memristor. (b) Schematics of the transport of carriers thought several sites that are modelled with energy barriers between them within a conductor. (c) Representation of a Type-I system and its signatures: a crossing in current-voltage characteristics at zero voltage, and the corresponding double values of conductance at this point. (d) Representation of a Type-II system and its signatures: the non-crossing current-voltage characteristics and the single conductance value at zero bias voltage.

These responses can be sorted into two main classes: the Type-I response presents a *self-crossing* behavior in the current-voltage characteristic, as displayed in the top panel of Fig. 1 (c), while Type-II presents a *non-crossing* one, shown in Fig. 1 (d) [18]. The existence of these two classes are important because from them, two different patterns of conductance arise. In Type-I, the conductance-voltage curves present two different values for the conductance at zero voltage, thus, two different conductive states that can be resolved in the lower panel of Fig. 1 (c); while Type-II presents only a single value of conductance at zero voltage, as represented in the lower panel of Fig. 1 (d).

1.1 Motivation

An important motivation for this Master project was the development of comprehensive models able to elucidate the nature of these responses. Part of it has already been provided and recently published as *"The Ubiquitous Memristive Response in Solids"* [1]. This paper describes a theoretical model that explains the memory formation in conductive

solids by carrier generation/trapping dynamics. It deals with sinusoidal voltage pulses although, in principle, the theory would also allow the implementation of the model for any type of applied voltages, at least numerically. Analytical expressions for the *non-equilibrium carrier number*, that are responsible for the *not-Ohmic behavior*, are presented. Also, the conductance's values of Type-I and II system at zero voltage; and the robustness of the memory response are presented. Besides, the model provides the analytical values of applied voltage frequencies able to maximize the memory responses of both Type-I and Type-II systems. [1] Furthermore, in this thesis we have extended the investigation to explore the memory aspects that arise when triangular voltage pulses are applied since they are a common feature in cyclic voltammetry measurements. Analogously to the sinusoidal case, we have obtained analytical expressions and show how a simple change in the shape of the applied bias is a sufficient condition for changing the response of the system. The results of both kinds of voltage inputs are compared, showing that although in general similar, the responses still present differences. In this way, the study of the memory emergence under different applied bias voltage provided insights about the memory formation process; and understanding the contrasts of their responses is a key issue for tuning memristive response.

This model was also successfully used to explain the memory formation in ZnO thin films and the effects of temperature, that is also included in this thesis. It resulted in the publication of the paper *"Temperature, detriment, or advantage for memory emergence: The case of ZnO"* in The Journal of Chemical Physics. [26] This work was part of a collaboration with experimental colleagues that fabricated and characterized the samples and their transport properties. Thus, this research foresees the development of a grounded physical model able of describing the memory formation in conductive solids with results that have been recently proven of value for the experimental characterization of various devices and systems.

Beyond all that, we have already introduce asymmetries in the model, that could be present in the energy barriers of its sites, elucidating how intrinsic features of the systems can affect its response, in contrast of the extrinsic ones (bias voltage: frequency and shape); and we have also started the investigations of the topology of the crossings in the current-voltage characteristics. These findings resulted in the publication of the paper *"Tuning the conductance topology in solids"* [27] that appeared as a *featured* paper in the *Journal of Applied Physics*. Furthermore, we have also extended the mathematical formulation of the model to deal with the generation of higher order modes, instead of using just the first order usually done; we have also introduced the definition of *impedance per mode* and we have demonstrated that apparent capacitive or inductive effects naturally emerge in these system, even in the absence of any magnetic elements. We have demonstrated the limitations of defining *equivalent circuits* for these kinds of systems; these results yielded the publication of the paper *"Inadequacy of equivalent circuits in nonlinear systems with*

inherent memory" [28].

Summarizing, the simple conduction model presented in this thesis proved to be very efficient in describing the nature of these systems. More than that, the model has been evolving with our current efforts, moving towards the exploration of topology and impedance features under a formulation of higher order modes. These topics are still ongoing and have already presented fruitful results, but are not yet closed topics. Finally, the model is also being extended, to explore the memory formation in quantum dots systems and also to explain rich memory features that arise in new ZnO doped thin films samples.

1.2 Goals and Methods

In this research project we have studied the memristive behavior that emerges in several devices according to different underlying physics of memory formation processes. Part of these efforts have been finished and some other continue running in communion with the specialization in the fabrication of structures and low-dimensional devices within a network of collaborators that combines theoretical and experimental expertise. The goals of this project, are:

1. To help developing theoretical models able of explaining the memory formation in conductive solids via generation/trapping dynamics of *non-equilibrium* carriers;

2. To provide a consistent description of memory emergence and its properties under the effect of temperature in ZnO thin films;

3. To perform simulations in order to investigate different voltage input pulses regimes and the operation of such memristive devices, foreseeing optimal responses.

The method adopted in this research combines studying the state of art of the scientific literature on this field, as well as the foundations of conductive mechanisms in solids. Based on the later, a theory has been built that provides clues for the natural memory emergence in conductive solids by generation or trapping of *non-equilibrium* carriers. The theory also provides analytical descriptions for memristive systems under certain limits of temperature or voltage amplitudes. Numerical calculations of the memory emergence have been performed in order to provide double checks of the analytical results or to go beyond the limits of the analytical approximations. The theoretical model has been built in close connection with experimental collaborators, which is important for attaining accuracy in describing what is observed in the experiments. Thus, the memory emergence in ZnO thin films and the temperature effects, unveiled for these structures, have already provided a good experimental confirmation of our predictions.

1.3 Thesis Overview

In order to provide a concise and comprehensive guideline of this thesis and to facilitate the reading through its logical structure and main ideas, we have organized it in five chapters, being the actual Chapter 1, the Introduction. Then, in the 2º Chapter, *Theoretical Background*, we have extended the Drude's model for conductivity in solids, in a perturbative way, by introducing and exploring the effects of *non-equilibrium* carriers that can be (*de*)activated, thus providing contributions to the conductivity. Namely, in Section 2.1, we have worked with the already established Drude's Theory for conduction in metals, culminating in the simple *Ohmic-expression* for the current density and conductivity; and in Subsection 2.1.1, we have performed all the calculations for modulating the thermal transport over an energy barrier, yielding expressions for the carrier flux over a barrier. Finally, in Subsection 2.2, we have indeed introduced the perturbation to the *Ohmic-conductivity* and worked on this perturbation term by modelling its dynamics induced by a generation function that is responsible for adding or subtracting new carriers to the system (if subjected to certain stimulus) in the presence of a *decay* term. The latter depends on a relaxation time and is proportional to the quantity of non-equilibrium carries present there. As these *generation functions* are unique for each material and their action mechanisms rely on the physical nature of the systems, we have also modeled a function that can by applied to *metal-semiconductors-metal* junctions (or vice-versa), and that operates by *thermal activation* of the carriers. Finally we have applied this function in Chapter 4, in order to describe the experimental results obtained in zinc oxide thin films experiments.

In Chapter 3, *Theoretical Results*, we have assessed four different theoretical systems in order to better understand the memory emergence mechanism and its properties. The models have been designed with generation functions simply proportional to the applied voltages (or their absolute values), we used *sinusoidal-like* or *triangular-like* pulses, and we were able to emulated memristive responses of Type I and II. The models have been organized in sections: 3.1 for the sinusoidal input with its extension beyond analytical validity regime by numerical methods in Subsection 3.1.1; and Section 3.2, for the triangular ones. This later being separated into Subsection 3.2.1, for Type-I response; 3.2.2, for Type-II; and 3.2.2.1, for comparing them. We performed analytical calculations that resulted in expressions for the non-equilibrium carries, conductance, currents, and *content* values. All the calculations have been double-checked by numerical methods. Figures of merit of the system response have been also presented, including the ones considered as a *signature of memory*: the *current-voltage hysteresis* curves.

In the 4º Chapter, *"Experimental confirmations and the effect of temperature in ZnO thin films"*, we have applied the model to predict and explain memory features that emerged in samples based on ZnO thin films, that were fabricated and characterized by colleagues, reinforcing its validity. It has been organized into two main parts. In Section 4.1 we have

basically adapted the triangular pulse model, with a generation function proportional to the voltage, to a new one, proportional to its second power. In Section 4.2, we indeed apply the model to the experimental results in order to explain them, extract useful intrinsic information of the system, and to predict its behavior under certain circumstances. Finally, in Chapter 5, the conclusions of this work, as well as, the perspectives and directions of the forthcoming research tasks are presented.

2 Theoretical Background

In this chapter we present the main theoretical concepts that allow describing conduction mechanism in solids, capable to also encompass the emergence of memory features. We also show, step by step, how our conduction memory model was built from basic ingredients. Namely, we have started, preliminarily, from the Drude's model of conductivity in solids. Then, by using the density of states, the Fermi Dirac distribution function in the non-degenerate limit, and assuming thermalized Maxwell fluxes of particles we have been able to calculate the carrier activation towards conductive states. Being this activation process the very core of our model able to explain the memory emergence in conducive solids. All the details and steps to formulate the theory are presented in the following sections.

2.1 Drude's Theory and Current Density

In its simplest form, the Drude theory of conduction in metals establishes a model for conduction based on the presence of a gas of free electrons, which move in a background of heavy ions. This electron gas is treated as dilute and neutral by using methods of the kinetic theory. Below, some important considerations about the model are listed:[1]

1. Each electron is assumed to move in a straight line between collisions, not interacting with other electrons or ions. And the non-electron-electron interaction represents the independent electron approximation; whereas the non-electron-ion interaction is the so-called free electron approximation.

2. Collisions are treated as instantaneous events, as in the kinetic theory, and are capable of abruptly changing the speed of electrons.

3. Collisions are modeled as happening with a probability given by $1/\tau$, where τ is called the *scattering time*.

4. The thermal equilibrium of electrons with their surroundings is achieved only through collisions. And it is assumed that, after a collision, the electron acquires a velocity that depends exclusively on the local temperature.[2]

We can define the proportionality factor between the applied electric field, $\vec{E}$, and the current density it induces, $\vec{j}$, as a characteristic constant of the material, the

[1] The assumptions can be seen in *Solid State Physics* [29], pages 2-5.

[2] It is worth of mentioning that alongside this thesis we have adopted the symbol T_{eff} for the temperature, in order to avoid confusion with the *period*, represented by T.

conductivity, σ:

$$\vec{j} = \sigma \vec{E}. \tag{2.1}$$

The current density, represents how much charge per unit time crosses perpendicularly a certain area of the material. Now, by considering a density of ρ electrons per unit volume and moving with a speed $\vec{v}$. Therefore, in dt time, the electrons advance a distance vdt in the direction of $\vec{v}$, so that $(n\, v\, dt\, A)$ electrons cross the area A. Given the charge $(-e)$ of the electrons, the charge element, dq, that crosses the area A in a time interval dt is given by $dq = -n\, e\, v\, A\, dt$. Therefore, the current density can be written as

$$\vec{j} = -\rho e \vec{v}. \tag{2.2}$$

Note that the speed $\vec{v}$ of the electrons represents an average value, which must be zero in the absence of an electric field. However, the application of an electric field $\vec{E}$ forces the electrons to acquire a non-zero average drift velocity $\vec{v}$ that points towards the opposite direction of the field, and in order to calculate this average speed one must consider that it does not depends on the speed of the electrons before a collision. Considering an electron just after a collision, then it will be subject to the electric field $\vec{E}$ and must travel a time τ before the next collision. Thus, the average change in momentum between two consecutive collisions is given by, $-eE\tau$. Therefore, the drift velocity acquired by the electron at the end of this process can be written as

$$\vec{v}_{avg} = -\frac{e\vec{E}\tau}{m}. \tag{2.3}$$

Therefore, from Eq. (2.2) we can write the current density as

$$\vec{j} = \left(\frac{\rho e^2 \tau}{m}\right) \vec{E}, \tag{2.4}$$

and the conductivity of the material is given by

$$\sigma = \frac{\rho e^2 \tau}{m}. \tag{2.5}$$

In the following steps we will consider that ρ in Eq. 2.5, representing a density of carriers per unit volume, may fluctuate around certain equilibrium value, ρ_0, given a non-equilibrium contribution, $\delta\rho$, that depends on time. The latter is generated by the activation or trapping of carriers.

2.1.1 Density of non-equilibrium carriers

The model for non-equilibrium carrier generation considered here consists of a thermal activation mechanism over energy barriers. They can be part of certain localized sites that can be related, for instance, to point defects, impurities, interfaces, grain

boundaries, etc. These sites may, in turn, act as nonequilibrium charge generators or traps and we will reduce this effect to one dimension in order to model their efficiency in terms of carriers fluxes in and out. Thus, the first basic ingredient of our model is the calculation of the flow of carriers through an energy barrier.

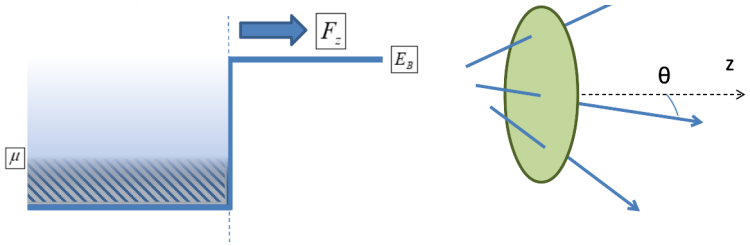

Figure 2 – Schematic representation of carriers activation over a barrier. The left panel represents a one dimensional energy barrier, E_B. The *quasi Fermi level* of the reservoir, located at the left side of the barrier, is represented by μ. The activated carriers pass over the barrier contributing to the one dimensional flux F_z. The right panel is a representation to reinforce that the net flux is calculated along direction z within the spherical coordinate system used in the model.

We can assume that this flow takes place along the z direction, as represented in Fig. 2. Then the carrier flux can be defined by using the local carrier density and their average velocity in the z direction as

$$F_z = \rho \langle v_z \rangle. \tag{2.6}$$

The average velocity of the carriers in z direction can in turn be obtained from a distribution function of speeds.

Although, as Fermions, electrons obey the Fermi-Dirac statistics, here we are going to assume the non-degenerate limit and approximate the system for the case in which the electron velocity distribution is given by the Maxwell-Boltzmann function. In this case, the expected value for the flow in the z direction is given by

$$F_z = \int d^3v \; \rho \; f_{MB}(\vec{v}, T_{eff}) v_z, \tag{2.7}$$

where f_{MB} is *Maxwell-Boltzmann Distribution Function*, given by:[3]

$$f_{MB}(\vec{v}, T_{eff}) = \left(\frac{m}{2\pi k_B T_{eff}} \right)^{3/2} \exp\left(-\frac{mv^2}{2k_B T_{eff}} \right). \tag{2.8}$$

Now, considering a spherical coordinate system, we can write v_z as

$$v_z = v \; \cos(\theta), \tag{2.9}$$

and in this spherical system the expression for F_z can be rewritten as

$$F_z = \int_{v=0}^{\infty} \int_{\theta=0}^{\pi/2} \int_{\phi=0}^{2\pi} d\phi \, d\theta \, dv \; \left(v^2 \sin(\theta) \right) \rho f_{MB}(v) \, v \cos(\theta). \tag{2.10}$$

[3] Where T_{eff} represents the effective temperature.

Note that $\int_0^{\pi/2} d\theta \sin\theta \cdot \cos\theta = \frac{1}{2}$, $\int_0^{2\pi} d\phi = 2\pi$ and by considering the density ρ as a constant, one obtains

$$F_z = \pi\rho \left(\frac{m}{2\pi k_B T_{eff}}\right)^{3/2} \int_{v=0}^{\infty} dv\, v^3 \, \exp\left(\frac{-mv^2}{2k_B T_{eff}}\right). \tag{2.11}$$

Now, we can focus our attention to calculate an expression for the average speed of the carriers where we have

$$\langle v \rangle = \iiint d^3v \, |v| f_{MB}(v), \tag{2.12}$$

so that,

$$\langle v \rangle = \int_{v=0}^{\infty} \int_{\theta=0}^{\pi} \int_{\phi=0}^{2\pi} d\phi \, d\theta \, dv \, \left(v^2 \sin(\theta)\right) f_{MB}(v)\, v, \tag{2.13}$$

because $\int_{\theta=0}^{\pi} d\theta \, \sin(\theta) = 2$ and $\int_0^{2\pi} d\phi = 2\pi$, and finally,

$$\langle v \rangle = 4\pi \left(\frac{m}{2\pi k_B T_{eff}}\right)^{3/2} \int_{v=0}^{\infty} dv\, v^3 \, \exp\left(\frac{-mv^2}{2k_B T_{eff}}\right). \tag{2.14}$$

Then, by contrasting Eqs. 2.11 and 2.14 we can write the flux of particles along z direction as a function of the expected value for their velocity as

$$F_z = \rho \frac{\langle v \rangle}{4}. \tag{2.15}$$

Thus, the next step to be performed consists of solving the integral of the expression for the expected value of the velocity, that is, solving an expression of the type

$$I_n = \int_0^{\infty} x^n \exp\left(-bx^2\right) dx. \tag{2.16}$$

Specifically we want to solve the case for $n = 3$

$$I_3 = \int_0^{\infty} x^3 e^{-bx^2} dx, \tag{2.17}$$

and in order to do that we may perform the following change of variables, where $\alpha \equiv x^2$ and $d\alpha = 2xdx$, yielding

$$I_3 = \frac{1}{2} \int_{\alpha=0}^{\infty} \alpha e^{-b\alpha} d\alpha \tag{2.18}$$

that, integrating by parts leads us to the result,

$$I_3 = \frac{1}{2b^2}. \tag{2.19}$$

Then Eq.(2.14), using $b = m/2k_B T_{eff}$, can be rewritten as

$$\langle v \rangle = \left(\frac{8k_B T_{eff}}{\pi m}\right)^{1/2} \tag{2.20}$$

Subsequently, we must find an expression for the volumetric carrier density ρ. For this, we assume the Fermi-Dirac distribution function, f_{FD}, and the density of state, $D(E)$

per unit volume, considering that the carriers available for transport are only those with energy larger than that of the barrier, E_B. So, we can write

$$\rho = \int_{E=E_B}^{\infty} D(E)\, f_{FD}(E,\mu)\, dE, \tag{2.21}$$

with,

$$\begin{cases} f_{FD}(E,\mu) = \dfrac{1}{1+\exp\left(\frac{E-\mu}{K_B T_{eff}}\right)} & (2.22) \\ D(E) = \dfrac{1}{L^3}\dfrac{\delta N_{\delta E}}{\delta E} = \dfrac{m^*}{\hbar^3\pi^2}\sqrt{2m^*\,(E-E_B)}. & (2.23) \end{cases}$$

This density of states, $D(E)$, was obtained from a quantum formalism for the treatment of electrons as follows. Considering a parabolic conduction band and the free electron approximation with an effective mass, m^*, we can set the time-independent Schrodinger equation, with a constant potential profile as

$$-\frac{\hbar^2}{2m^*}\nabla^2\vec{\psi}(\vec{r}) = (E-U_0)\,\vec{\psi}(\vec{r}). \tag{2.24}$$

Then, considering periodic boundary conditions (*Born-von Karman* conditions) we obtain plane wave solutions for the electrons and a dispersion relation for the energy, which in the one-dimensional case (for simplicity) would be

$$\begin{cases} \psi = \dfrac{e^{ik\cdot z}}{\sqrt{L}} & (2.25) \\ E - U_0 = \dfrac{\hbar^2 k^2}{2m^*}, & (2.26) \end{cases}$$

where L is the length between boundaries. By applying this solution to the *Born-von Karman* conditions, we obtain a quantization condition for the allowed values of k, $k_n = \frac{2\pi\cdot n}{L}$. Taking the limit $L \to \infty$ we can write the difference between two allowed values of k as a differential element, $dk = k_n - k_{n-1} = \frac{2\pi}{L}$.

Thus, we can define a density of allowed energy states δN as the number of allowed values of k, δK, in an interval dk. That is, $\delta N = \frac{\delta k}{dk} = \frac{L}{2\pi}\delta k$. And taking into account the spin degeneracy, each value of k represents two energy levels for electrons, so

$$\delta N = 2\cdot\frac{\delta k}{dk} = \frac{L}{\pi}\delta k. \tag{2.27}$$

Now, from the dispersion relation Eq. (2.26), for each k we have two energy values, i.e. $\delta N_{\delta E} = 2\cdot\delta N_{\delta k}$. And as $\delta E = \frac{dE}{dk}\cdot\delta|k| = \sqrt{\frac{2\hbar^2}{m^*}}\sqrt{E}\cdot\delta|k|$. Then, the number of states within δE as a function of energy becomes

$$\delta N_{\delta E} = \frac{L}{\hbar\pi}\sqrt{\frac{2m^*}{\hbar}\frac{1}{E}}\cdot\delta E. \tag{2.28}$$

For the case in three dimensions, we proceed in a completely analogous way considering the space isotropy. We have $dk = \frac{2\pi}{L}$ and $\delta N = 2\cdot\frac{\delta^3 k}{8\pi^3/L^3}$, with $\delta^3 k = 4\pi|k|^2\cdot\delta|k|$,

in spherical coordinates. So, $\delta E = \frac{\hbar^2|k|}{m^*} \cdot \delta|k|$, and we can write the 3D state count as a function of energy as

$$\delta N_{\delta E} = \frac{L^3 \cdot m^*}{\hbar^3 \pi^2} \sqrt{2m^* E} \cdot \delta E, \tag{2.29}$$

and the *density of states* expression is obtained by taking the ratio of the above expression per unit energy and unit volume, L^3.

Now, returning to the calculation of the number of occupied states, solving Eq.(2.21), we get

$$\rho = \frac{m^*}{\hbar^3 \pi^2} \sqrt{2m^*} \int_{E=E_B}^{E=\infty} \frac{(E - E_B)^{-1/2}}{1 + \exp\left(\frac{E-\mu}{k_B T_{eff}}\right)} dE, \tag{2.30}$$

and considering again the nondegenerate limit with the approximation that $E - \mu >> k_B T_{eff}$, we have

$$\rho = 2 \left(\frac{2\pi m^* k_B T_{eff}}{(2\pi\hbar)^2} \right)^{3/2} \cdot \exp\left(-\frac{E_B - \mu}{k_B T_{eff}} \right). \tag{2.31}$$

From the equations (2.15) and (2.31), we can write the expression for the FLUX in the z direction as

$$F_z = \frac{4\pi m^* k_B^2 T_{eff}^2}{(2\pi\hbar)^3} \exp\left(-\frac{E_B - \mu}{k_B T_{eff}} \right) \tag{2.32}$$

Now, to generalize this model, let's imagine the charge activation process happening on both sides of a barrier, as represented in Figure 3.

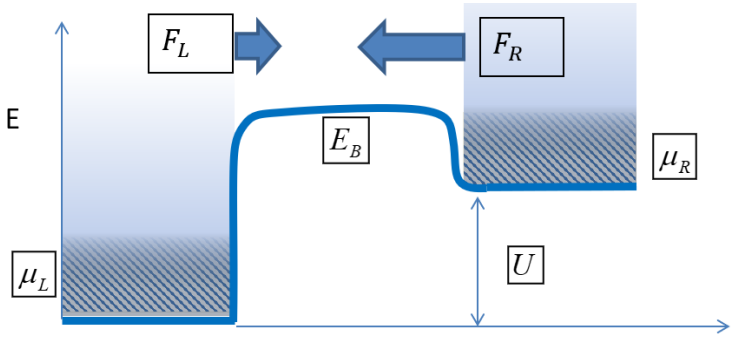

Figure 3 – Schematic representation of a energy barrier. At the left and right side of it, it is depicted the chemical potentials μ_L and μ_R, respectively. The energy barrier E_B separates these two regions, with the chemical potential on the right side given by $\mu_R = U + \mu_L$ and $U = -|e|V$. F_L represents the carriers flux that goes from the left reservoir to the right one over the barrier; in an analogous way, F_R represents the carrier flux from the right to the left side. In case we are dealing with electrons, due to its negative charge, if one wants to write their current densities, they will be represented with a inversion in the direction of their respective fluxes.

See that $\mu_R \equiv \mu_L + U$, with U modelling a displacement in the energy profile of the device that is caused by the applied bias voltage, i.e. $U = -|e|V$. Thus, left and right fluxes can be written as

$$\begin{cases} F_L = \dfrac{4\pi m^* k_B^2 T_{eff}^2}{(2\pi\hbar)^3} \exp\left(-\dfrac{E_B - \mu_L}{k_B T_{eff}} \right), & (2.33) \\ F_R = -\dfrac{4\pi m^* k_B^2 T_{eff}^2}{(2\pi\hbar)^3} \exp\left(-\dfrac{E_B - \mu_R}{k_B T_{eff}} \right). & (2.34) \end{cases}$$

and the net flux in z direction, F, obtained by the addition of the previous terms as

$$F = \frac{4\pi m^* k_B^2 T_{eff}^2}{(2\pi\pi)^3} \exp\left(-\frac{E_B - \mu_L}{k_B T_{eff}}\right)\left[1 - \exp\left(\frac{U}{k_B T_{eff}}\right)\right]. \tag{2.35}$$

Note that Eq.(2.35) models the flux produced by thermal activation between two regions with different chemical potentials, μ_L and $\mu_R = U + \mu_L$, with the presence of an energy barrier E_B between them and a applied bias voltage V.

In order to recap, Eq. 2.35 has been obtained by means of a semiclassical formulation: while the speed of electrons have been modeled by using the classical Maxwell-Boltzmann distribution, the Fermi-Dirac function, of quantum mechanics, have been used to calculate the electron occupation of the energy levels. Besides, the validity of Eq. 2.35 is true for a high enough energy E of the electrons or, equivalently, for sufficiently low temperatures, i.e. $\frac{E-\mu}{k_B T_{eff}} \ll 1$.

Now, in the following section 2.2, we use the ideas and the formalism of Eq.(2.35), that describes thermalized Maxwell fluxes through a *single* barrier, as the basis for building a carrier generation mechanism in solid conductors. This mechanism, as it will be seen, has been modeled by using the fluxes of particles description but now applied to *double barrier regions*, that will play the role of *generation* or *trapping* sites.

2.2 The model used to study the memory emergence

Under an electric field, E, within the mean free time approximation, τ, and a wide temperature range, the current density in solids can be described by the Drude like formalism, where the main contribution is provided by carriers at the Fermi energy. Thus, the conductivity itself becomes proportional to the carrier concentration: $\rho = \rho_0 + \delta\rho$, like in Eq. 2.4,

$$j = e^2\tau/m^* \left(\rho_0 + \delta\rho\right) E. \tag{2.36}$$

Here we have singled out the perturbative contribuition of nonequilibrium carriers, $\delta\rho$, that can be promoted to or removed from conductive states by a combination of photogeneration, heating, and/or external fields, as represented in Fig. 4 (a) under an applied bias voltage. In terms of current, $I = jA$ (A- cross-section area), driving voltage V, and number of nonequilibrium carriers in the volume Ω, $\delta n \equiv \delta\rho\,\Omega$, Eq. 2.36 can be translated as $I = (G_0 + \alpha\,\delta n)\,V$, where G_0 represents the conductance of the unperturbed system. Then, given the size, a_z, of the segments where nonequilibrium charges are generated or trapped, as displayed in Fig. 2 (a), and the distance between contacts L_z, the local voltage drop at each generation or trapping site is defined as ηV, with $\eta = a_z/L_z$.

For simplicity, we will consider a single transport channel with just electrons or holes that can be generalized afterwards to more complex combinations. Then, the fluctuating

δn under the influence of external perturbations can be emulated by using the relaxation time approximation

$$\frac{d\,\delta n(t)}{dt} = g(V) - \delta n(t)/\tau, \tag{2.37}$$

with $g(V)$ being the voltage dependent generation rate and τ - the non-equilibrium carriers lifetime that rules the relaxation process. One may thus assume that the carrier generation can be thermally activated and/or induced by light absorption.

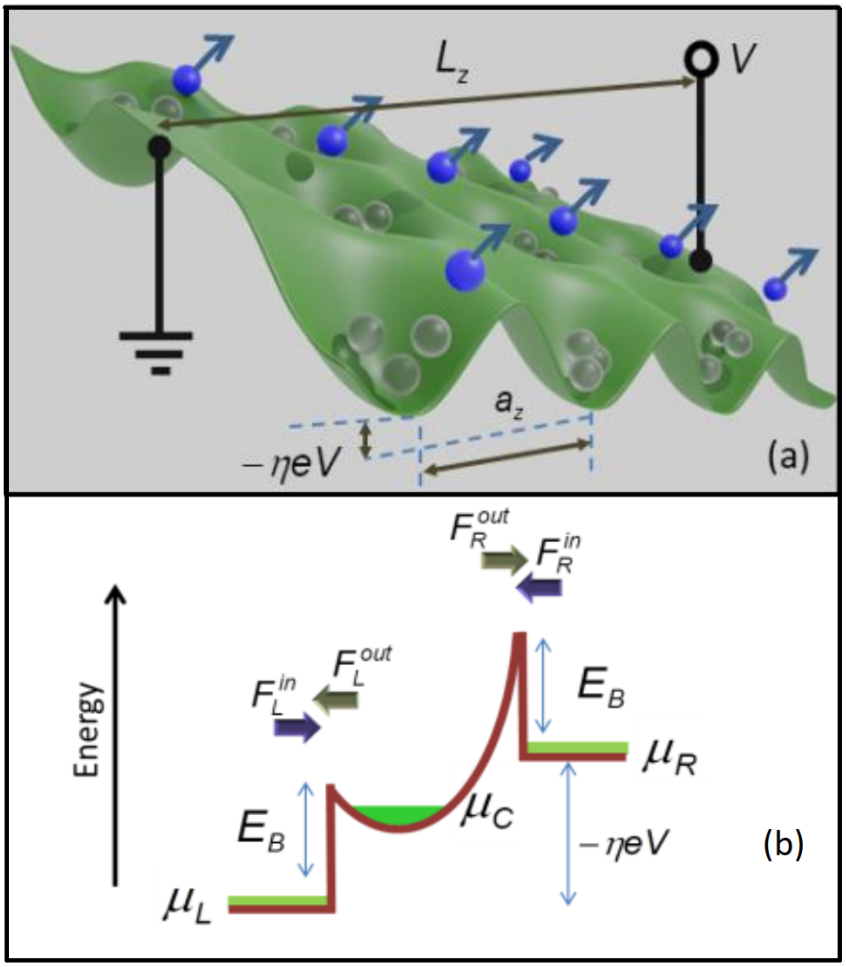

Figure 4 – (a) Schematic diagram representing the activation of trapped non-equilibrium carriers under external voltage and the local bias determined by the efficiency η, that is related with the density of generation sites in the material, namely: $\eta = Site\ Length/Total\ length$ (b) Diagram representing trapping site with metal-semiconductor-metal profile and the mechanism of promoting carriers to the conduction band by thermal excitation.

The effective energy profile, assuming axial symmetry along the transport direction, has been displayed in Fig. 4 (b), where the nonequilibrium charge dynamics will be driven by the relative heights of left and right effective barriers that modulate the particle fluxes at each side of the trapping site, represented by arrows. The incoming (in) and outgoing (out) components of Maxwell particle fluxes over each side of the barriers can be calculated (according to Eq. 2.15) as $F_{L(R)}^{in(out)} = \delta\rho_{L(R)}^{in(out)}\langle v\rangle/4$, where $\delta\rho_{L(R)}^{out(in)}$ is the particle density at

the given interface[4] and $\langle v \rangle$ is the mean value of the thermal velocity, exactly as discussed in Section 2.1. [30]

Thus, considering a given carrier effective temperature, T_{eff} [31], and using Equations. (2.33, 2.34) for the fluxes over a barrier, one obtains

$$F_L^{in} = F_R^{in} = \frac{4\pi m^* \left(k_B T_{eff}\right)^2}{\left(2\pi\hbar\right)^3} \exp\left(-\frac{E_B}{k_B T_{eff}}\right), \tag{2.38}$$

and

$$F_{L(R)}^{out} = \frac{4\pi m^* \left(k_B T_{eff}\right)^2}{\left(2\pi\hbar\right)^3} \exp\left(-\frac{E_B + \mu_{L(R)} - \mu_C}{k_B T_{eff}}\right). \tag{2.39}$$

For the cross section, S, and a given number of localization sites along the direction between contacts, $1/\eta$, the total generation rate of non-equilibrium carriers becomes

$$g = \frac{S}{\eta}\left(F_L^{out} - F_L^{in} + F_R^{out} - F_R^{in}\right). \tag{2.40}$$

Then, given the lack of any preferential direction or intrinsic gradients within the effective profile of Fig. 4 (b), we can further impose the symmetry constraint, $\mu_R - \mu_C = \mu_C - \mu_L$, that reduces $g(V)$ to

$$g(V) = \frac{i_0}{\eta}\left[\exp\left(-\frac{\eta e V}{2k_B T_{eff}}\right) + \exp\left(\frac{\eta e V}{2k_B T_{eff}}\right) - 2\right], \tag{2.41}$$

with $i_0 = \frac{4\pi m^* \left(k_B T_{eff}\right)^2}{\left(2\pi\hbar\right)^3} \exp\left(-\frac{E_B}{k_B T_{eff}}\right)$. Note that we have assumed μ_C as the source of nonequilibrium carriers. In case μ_L and μ_R were the sources, it suffices to invert the sign of i_0 in Eq. (2.41). We may also introduce another generation function that is used for single junctions or *diode-like* responses, given by

$$g(V) = g_0 + \frac{i_0}{\eta}\left[1 - \exp\left(-\frac{\eta e V}{k_B T_{eff}}\right)\right]. \tag{2.42}$$

Thus, the combination of these basic ingredients, namely: **1)** the existance of *non-equilibrium* carriers and **2)** their dynamics, that is driven by a generation function and a decay term; can be proven to be sufficient condition for the emergence of memory in the transport properties of solids, as it is shown in Chapter 3.

The generation function of Eq. 2.42 was used as inspiration for the construction of the models that have been presented in Chapter 3. In this Chapter, many insights of memory emergence features are explored and presented. Finally, in Chapter 4, the generation function of Eq. 2.41 will serve as the basis for the theory used to describe and predict results in samples of ZnO thin films that were built and characterized by colleagues. The good agreement of theory and experiment presented there points to the robustness of the model.

[4] In order to avoid mistakes, note that while $\delta\rho$ is the non equilibrium carrier density, δn represents the effective non-equilibrium carriers number.

3 Theoretical results

In this chapter, we have explored the features of our conductance model that is subjected to distinct generation functions and voltage inputs. This resulted in four cases, that provided a rich amount of results and insights about the memory formation and its properties. In all those results, the inspiration for building the generation functions came from the *Diode-like* function of Eq. 2.42. By approximating this function up to first order terms in voltage we have been able to produce compact analytical solutions. This case yielded a Type-I response as demonstrated in the following section. Extrapolating a little further, we have also built other model where the generation function, was also taken to the first order in voltage of but a symmetry was imposed by taking its *absolute value*. This later case was used to highlight the memory emergence of a Type-II response.

This Chapter is organized in the following manner: In Section 3.1 we present the results for systems driven by both cases of generation function, under a periodic sinusoidal bias voltage. We deduce and explore their properties analytically, comparing the differences in the responses that arises by the symmetry change of the generation functions. After that, in Subsection 3.1.1, we extrapolate the analytical results by numerical methods and assess the strength of the analytical model out of its validity regime.

Subsequently, in Section 3.2 we proceed in a similar way, with the same two kinds of generation functions, but now studying the response under a triangular voltage input. The results in this chapter are novel and provide interesting insights about the memory formation, demonstrating how a simple change in the form of the input can drastically affect the response of a memristive system (once it is compared with the previous responses of the sinusoidal section). The triangular Type-I and II models are developed in details in Subsections 3.2.1 and 3.2.2, respectively; while in 3.2.2.1 the results are compared, and figures of merit are presented.

3.1 Sinusoidal input

Let us first consider the *diode-like* generation rate of Eq. 2.42 within the relative low voltage approximation, when $\frac{\eta eV(t)}{k_B T_{eff}} << 1$. In this case, and neglecting terms beyond first order in voltage, Eq. 2.42 reduces to $g(V) = g_0 + \sigma V(t)$, with $\sigma = i_0 e/k_B T_{eff}$. Two basic sets of responses can then be distinguished corresponding to Type-I and II, with generation rates $g^{I(II)}(V) = g_0 + \sigma V^{I(II)}(t)$. According to the diagrams in Fig. 1: Type-I corresponds to an asymmetric system, where the nonequilibrium transport contribution can be activated or deactivated according to the voltage sign, $V^I(t) = V(t)$, and Type-II, which is simply symmetric and thus independent of the voltage polarity, $V^{II}(t) = |V(t)|$.

Hence, in the linear response approximation, Eq. 2.37, for each type of dynamics, reduces to [1]

$$d\delta n^{I(II)}/dt = g_0 - \delta n^{I(II)}/\tau + \sigma V^{I(II)}(t). \tag{3.1}$$

Solving Eq. 3.1 for sinusoidal voltage pulses we obtain analytical expressions for the carrier number as a function of time, before and after a steady regime is set.

For the transient response, we can write the solution of the Type-I system (asymmetric) as a simple equation while, for Type-II (the symmetric one), it can be provided in a recursive form; namely [1]

$$\begin{cases} \delta n^{I}(t) = \left[\delta n_0 - g_0\tau + \dfrac{\sigma\tau V_0\omega\tau}{1+(\omega\tau)^2}\right] e^{-t/\tau} + g_0\tau + \dfrac{\sigma\tau V_0}{\sqrt{1+(\omega\tau)^2}}\sin(\omega t - \varphi) & (3.2) \\ \delta n_j^{II}(\mathfrak{T}) = \left[n_{j-1}^{0} - g_0\tau + \dfrac{\sigma\tau V_0\omega\tau}{1+(\omega\tau)^2}\right] e^{-\mathfrak{T}/\tau} + g_0\tau + \dfrac{\sigma\tau V_0}{\sqrt{1+(\omega\tau)^2}}\sin(\omega\mathfrak{T} - \varphi) & (3.3) \end{cases}$$

where the initial conditions are $n_1^I(0) \equiv n_0$ and $n_1^{II}(0) \equiv n_0$, with $\varphi \equiv arctan(\omega\tau)$. Also, for the case of the Type-II system, the index j = 1, 2, 3, . . . enumerates each voltage semicycle with the time variable, $\mathfrak{T}$, defined within a semiperiod range, $\mathfrak{T} \in [0, T/2]$ with

$$n_j^0 = L\coth\left(\frac{T}{4\tau}\right)\left(1 - e^{-j\frac{T}{2\tau}}\right) + n_0 e^{-j\frac{T}{2\tau}}, \tag{3.4}$$

Being L a parameter defined as

$$L \equiv \sigma\tau V_0\omega\tau / \left[\left(1+(\omega\tau)^2\right]\right. \tag{3.5}$$

By waiting enough time, the first decay terms vanish and a steady state is reached where the solutions become independent on the initial conditions and can be written, for Type-I and II systems, as [1]

$$\begin{cases} n_\infty^I(t) = g_0\tau + \dfrac{\sigma\tau V_0}{\sqrt{1+(\omega\tau)^2}}\sin(\omega t - \varphi), & (3.6) \\ n_\infty^{II}(\mathfrak{T}) = g_0\tau + \dfrac{e^{-\mathfrak{T}/\tau}}{1+(\omega\tau)^2}\dfrac{2\sigma\tau^2\omega V_0}{1-\exp\left(-\frac{\pi}{\omega\tau}\right)} + \\ \qquad \dfrac{\sigma\tau V_0}{\sqrt{1+(\omega\tau)^2}}\sin\left(\omega\mathfrak{T} - \varphi\right). & (3.7) \end{cases}$$

with, $\mathfrak{T}$ in the range $[0, T/2]$ and

$$\varphi \equiv \tan^{-1}(\omega\tau). \tag{3.8}$$

The resulting time dependence has been displayed in Fig. 5 (a), including the transient regime. The current for each type of system under the stabilized condition can thus be calculated as

$$I_\infty^{I(II)} = \left[G_0 + \alpha\,\delta n_\infty^{I(II)}(t)\right] V(t). \tag{3.9}$$

[1] Where g_0 corresponds to a constant in the generation function, that could be attributed, for instance, to a light excitation term of non-equilibrium carriers.

They are displayed, for the steady state regime, as function of time, in Fig. 5 (b) and as current-voltage $I - V$ characteristics in Figs. 5 (c) and (d). One may note that the hysteresis of Type-I system is asymmetric, while Type-II shows a symmetric behavior. The Figures 4 (e) and (f) present the asymptotic functional form of I - V characteristics in the limit of very slow or fast drives, respectively. They point to the hysteresis collapse for both systems in the limits of zero (DC pulse) or infinite frequency. The latter yielding *Ohmic* responses.

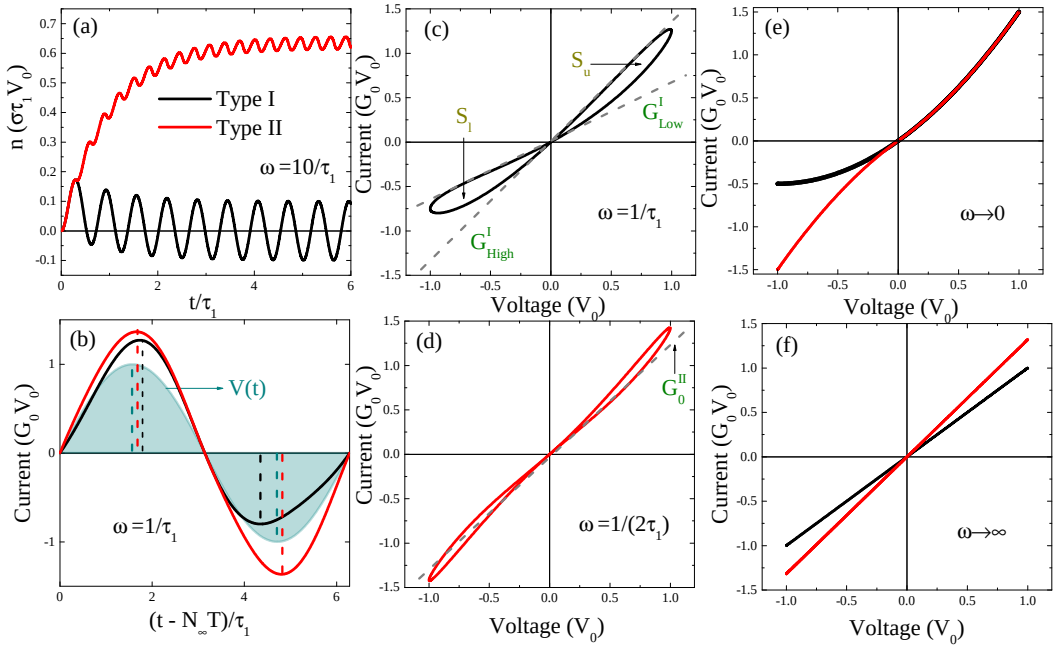

Figure 5 – Response difference between Type I (black lines) and Type II (red lines): (a) Transient towards the steady dynamics of nonequilibrium charge carriers under an AC voltage. (b) Current as a function of time for type I and II systems, in steady state regime. Here, N_∞ represents a sufficiently high number of periods for stability to be achieved. A solid pattern of a period of the voltage sweeps has been added in the background. (c) Type I current voltage characteristics after stability. The conductance values, G^I_{Low} and G^I_{High}, at zero bias are indicated by dashed lines while S_u and S_l label the areas of the upper and lower $I - V$ loops, respectively. (d) Type II current voltage characteristics after stability with a single conductance value, G^{II}_0, at zero bias indicated by a dashed line. (e) Stable $I - V$ response under an adiabatic voltage supply for type I and II systems. (f) Stable $I - V$ response under fast voltage oscillations for Type I and II systems.

Note, in Fig 6 (a), the sharp contrast between the conductance loops as functions of applied bias. While Type-I systems present two different values of conductance at zero voltage, an important feature for memcomputing functionalities; the Type-II systems present only a single one. This contrast can be tuned with the frequency of the voltage drive as depicted in Fig. 6 (b). According to this picture, the difference between *on* (high) and *off* (low) conductance states in Type-I systems collapses for low or high frequencies and it can be explicitly written as

$$\frac{G^I_{\infty,\mathrm{High}}(\omega) - G^I_{\infty,\mathrm{Low}}(\omega)}{\alpha\sigma\tau V_0} = \frac{2\omega\tau}{1+(\omega\tau)^2}, \tag{3.10}$$

pointing to a maximum on-off difference once $\omega\tau = 1$. In turn, for Type-II systems, the single conductance value at zero voltage is given by

$$\frac{G^{II}_{\infty,0}(\omega) - G_0}{\alpha\sigma\tau V_0} = \frac{\omega\tau}{1+(\omega\tau)^2}\coth\left(\frac{\pi}{2\,\omega\,\tau}\right), \tag{3.11}$$

with a monotonic growth that has also been represented in Fig. 6 (b).

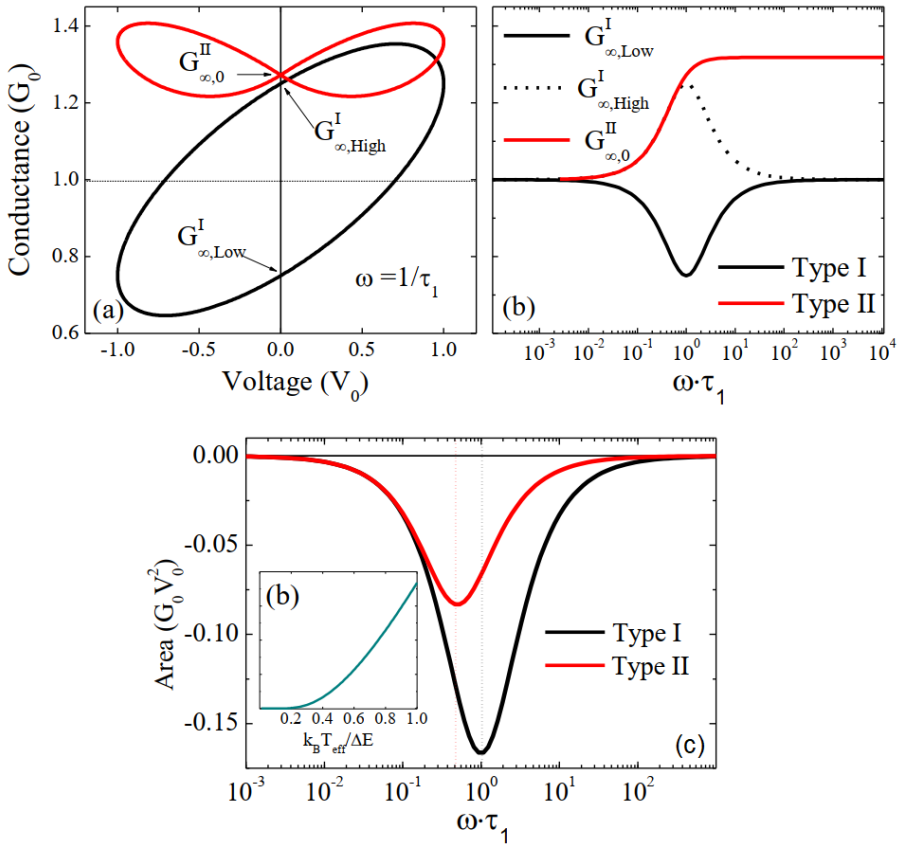

Figure 6 – (a) Conductance as a function of voltage, after reaching stability. (b) Conductance at zero voltage as a function of normalized angular frequency of the applied voltage within the linear approximation, under stable cycles, for the high (on) and low (off) conductance states of Type-I systems, represented in black; and for Type-II systems, in red. (c) Calculated current-voltage loop areas for both types of systems and (on the inset) expected evolution of the loop area (in absolute arbitrary units - valid for Type-I and Type-II) with increasing temperature.

Another relevant parameter used for the characterizations of the memristive response are the *Content Values*, that are represented by the areas of semi-loops of the current-voltage characteristics. It is used to measure the strength of the system memories properties. The definition of *Content* for the upper, $S_u^{I(II)}$, and lower, $S_l^{I(II)}$, loops are

$$S_u^{I(II)} = \int_{t'=0}^{t'=T/2} I_\infty^{I(II)} dV \;\text{ and }\; S_l^{I(II)} = \int_{t'=T/2}^{t'=T} I_\infty^{I(II)} dV. \tag{3.12}$$

In the case of sinusoidal voltage inputs, explicit expressions can be obtained that become figures of merit of our model. For Type-I they are

$$\frac{S_u^I}{(2/3)\alpha\sigma\tau V_0^3} = -\frac{S_l^I}{(2/3)\alpha\sigma\tau V_0^3} = -\frac{\omega\tau}{1+(\omega\tau)^2}, \tag{3.13}$$

and for Type-II

$$\frac{S_u^{II}}{(2/3)\alpha\sigma\tau V_0^3} = \frac{S_l^{II}}{(2/3)\alpha\sigma\tau V_0^3} = -\frac{\omega\tau}{1+(2\omega\tau)^2}, \tag{3.14}$$

depicted in Fig. 6 (c). One can see in Fig. 6 (c) that the memory strength of Type-I and II systems can be boosted by tuning the values of the applied voltage frequency. In Type-I systems, the maximal response happens at a higher frequency of applied voltage, namely $\omega = 1/\tau$; while, a lower frequency of $\omega = 1/2\tau$ is needed to obtain the maximum area of Type-II systems. Both *Content* values, however, increase with increasing temperature under the current hypothesis, as depicted in the inset of Fig. 6 (c).

3.1.1 Analytical Result Accuracy Beyond its Validity Regime

As mentioned in the beginning of Section 3.1, the validity of the linear approximation occurs whenever $\frac{\eta eV(t)}{k_B T_{eff}} \ll 1$. But we have also calculated the model response for conductivity and *content* numerically beyond the analytical regime. [1] What we want to show here is that although the model does not yield perfect results outside its validity regime, as expected, it does provide strikingly useful information for optimal tuning even outside the analytical approximation, as it can be seen in Figures 7 and 8.

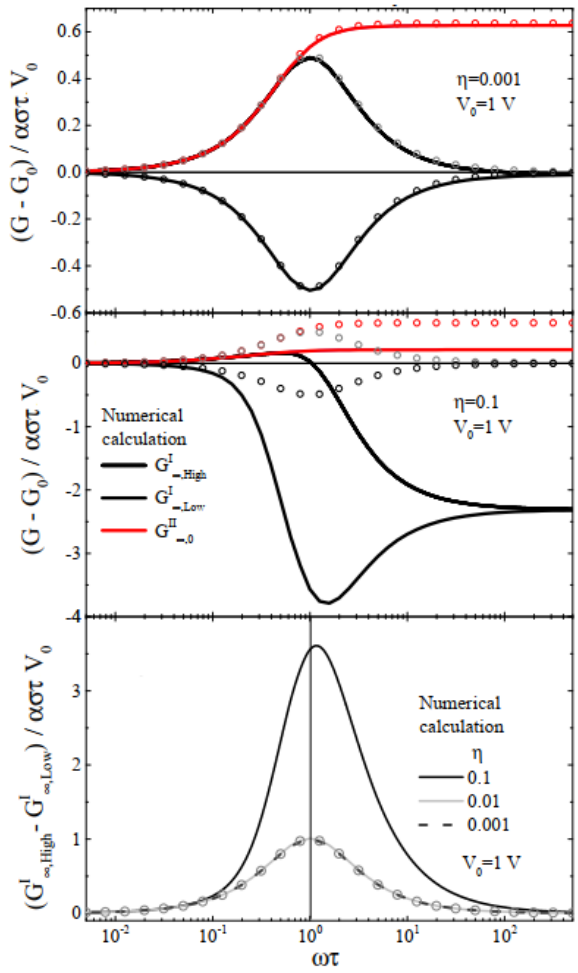

Figure 7 – This figure shows the normalized conductance as a function of $\omega\tau$, for the first two images. The black color is used to represent the Type-I system, while the red one, the Type-II. Points are used to indicate the analytical results from the linear approximation and the lines were obtained by means of numerical calculations. In the third picture the normalized difference is depicted between the states *High* and *Low* conductance of the Type-I system, for different values of η. Note also that for $\eta = 0.01$ (continuous representation) and $\eta = 0.001$ (dashed representation) the curves almost coincide.

In the sequence of images in Figure 7 we have depicted in black the values corresponding to Type-I system, and in red, the ones for Type-II. The dots indicate the analytical solution of the conductance for the first order approximation, while the lines represent the numerical results. It can be seen, in the first image, that for a very low η the system obeys the linear approximation regime and the analytical results coincide with the numerical ones. In the second image, η is not small enough in order to force the system to operate under the linear approximation, thus the dotted analytical results differ from the numerical ones. And in the third picture, we have depicted the normalized difference between the zero conductance states of Type-I system, as a function of $\omega\tau$ for different values of η. The remarkable conclusion here is that even beyond the condition when the first order approximation fails, the position of $\omega\tau$ that leads to the optimal memory response does not change drastically. In other words, the linear approximation

provides strong clues for finding the optimal external tuning parameters (frequency, ω, in this case), even for large voltage amplitudes or for systems that extrapolate the linear approximation. Namely, the optimal response for maximizing the *on-off* ratio of Type-I conductance occurs at $\omega = 1/\tau$. In a similar way, Figure 8 also indicates that even when a system does not obey the linear approximation regime, the location of their maximum *content* values remain around the location expected for the linear analytical result, i.e., for the Type-I system, the content is maximized at $\omega = 1/\tau$; while, for the Type-II, for $\omega = 1/2\tau$.

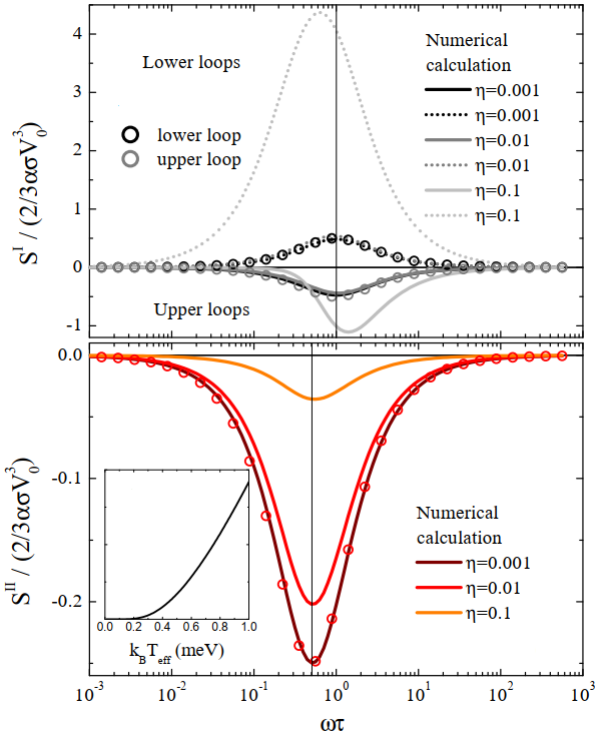

Figure 8 – In the upper image the upper and lower current-voltage areas of Type-I system are depicted for several values of η, that are represented by lines, while the dots represent the values obtained from the linear analytical approximation. In a similar way, the lower picture shows the results for the Type-II symmetrical system. While, in the inset, the expected evolution of the loop area is represented (in absolute arbitrary units valid for Types-I and II) with increasing temperature. This Figure were edited from [1].

3.2 Triangular input

In analogy to the sinusoidal voltage input investigations, we consider again a single transport channel with just electrons or holes, with δn representing the non equilibrium carriers that appear under external perturbation and are given by a rate equation like Eq. (2.37). Again, we consider the *diode-like* generation rate of Eq. (2.42) within the relative low voltage approximation, when $\frac{\eta eV(t)}{k_B T_{eff}} << 1$. In this case, and neglecting terms above first order in voltage, Eq. 2.42 reduces to $g(V) = g_0 + \sigma V(t)$, with $\sigma = i_0 e/k_B T_{eff}$. Two basic sets of responses can then be distinguished corresponding to Type-I and II, with

generation rates $g^{I(II)}(V) = g_0 + \sigma V^{I(II)}(t)$.

The difference consists is the introduction of a triangular voltage pulses, as represented in Fig. (9), as used for the cyclic voltammetry measurements. The voltage can be described as

$$V_{Triangular}(\mathfrak{T}) = \begin{cases} \dfrac{4V_0}{T}\mathfrak{T}, & 0 \leq \mathfrak{T} \leq T/4 \\ 2V_0\left(1 - \dfrac{2\mathfrak{T}}{T}\right), & T/4 \leq \mathfrak{T} \leq 3T/4 \\ \dfrac{4V_0}{T}\left(\mathfrak{T} - T\right), & 3T/4 \leq \mathfrak{T} \leq T \end{cases}, \tag{3.15}$$

where $\mathfrak{T}$ is a time variable, namely, a time that starts in the beginning of a cycle and ends in the end of it. In another words, if t is the *usual* time variable, so $\mathfrak{T} \equiv \text{Remainder}(t/T)$.

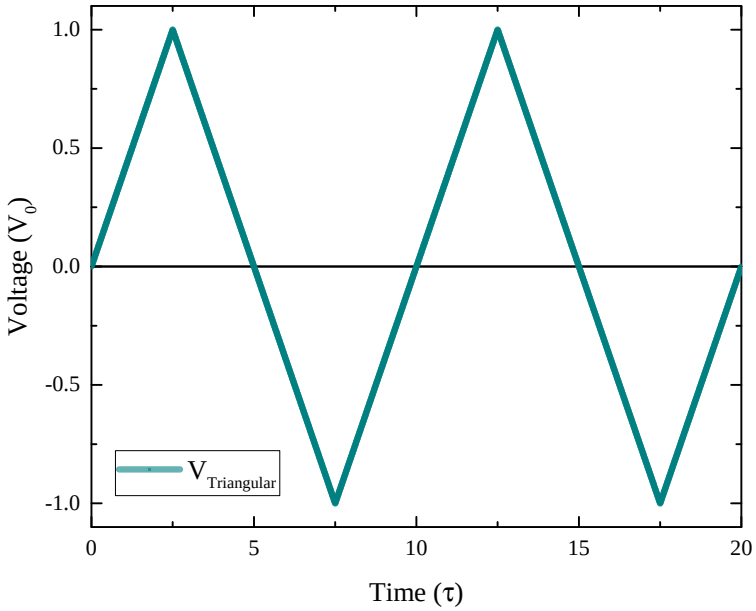

Figure 9 – Voltage $V_{Triangular}$ with a period $T = 10\,\tau$.

So, we can rewrite the generation function in a more explicit notation, as

$$g^{I(II)}_{Tri}(V_{Tri}) = \sigma_{1(2)} V^{I(II)}_{Tri}(t), \tag{3.16}$$

where, for simplicity, we have eliminated contribution of g_0 that could be attributed to a constant generation rate induced by light, for instance. Furthermore, $V^{I}_{Tri} \equiv V_{Triangular}$, while $V^{II}_{Tri} \equiv |V_{Triangular}|$, namely

$$V^{II}_{Tri} = \begin{cases} \dfrac{4V_0}{T}\mathfrak{T}, & 0 \leq \mathfrak{T} \leq T/4 \\ 2V_0\left(1 - \dfrac{2\mathfrak{T}}{T}\right), & T/4 \leq \mathfrak{T} \leq T/2 \end{cases}, \tag{3.17}$$

where the time variable, $\mathfrak{T}$, represents in this case the time within each *semiperiod* $T/2$, or $\mathfrak{T} \equiv \text{Remaider}(t/(T/2))$, and V^{II}_{Tri} is represented in Fig. (10).

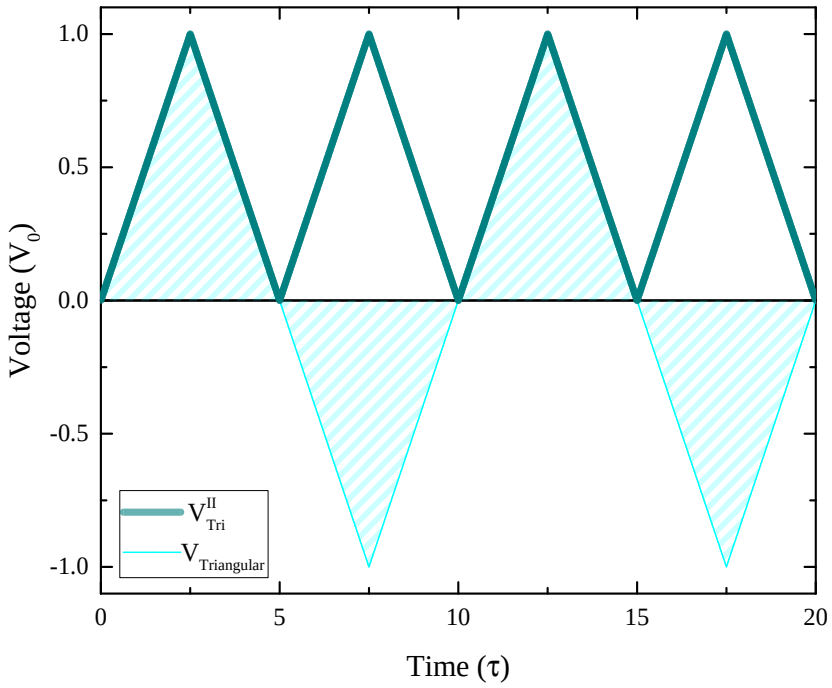

Figure 10 – Voltage V_{Tri}^{II} normalized, with a period $T = 10\,\tau$ in dark cyan, while the corresponding $V_{Triangular}$ normalized is shaded represented in cyan color.

3.2.1 Type-I System

We look for solutions of the following differential equation

$$\frac{d\delta n(t)}{dt} = -\frac{\delta n(t)}{\tau} + \sigma_1 V_{Tri}^{(I)}(t). \tag{3.18}$$

In this case we have to solved the system within three different regions, that are defined as

$$First \equiv \left\{\mathfrak{T},\ \mathfrak{T} \in \left[0, \frac{T}{4}\right]\right\}, \tag{3.19}$$

$$Second \equiv \left\{\mathfrak{T},\ \mathfrak{T} \in \left[\frac{T}{4}, \frac{3T}{4}\right]\right\}, \tag{3.20}$$

$$Third \equiv \left\{\mathfrak{T},\ \mathfrak{T} \in \left[\frac{3T}{4}, T\right]\right\}, \tag{3.21}$$

with $\mathfrak{T}$ being the effective time inside each complete cycle i, i.e. $\mathfrak{T} \equiv \text{Remaider}(t/T)$, or equivalently, $t \equiv i\,T + \mathfrak{T}$, with $i \in \mathbb{N}$, and the index i labels the number of complete cycles, starting with $i = 0$.

Before solving the system within each region, in order to simplify the results, lets define the constant a_1 that will appear frequently in the calculations

$$a_1 \equiv \frac{4\sigma_1 V_0}{T}, \tag{3.22}$$

thus, solving 3.18 for each region, one obtains

$$\delta n_i^{First}(\mathfrak{T}) = \left[\delta n_i^{0,\ First} + a\tau^2\right] e^{-\mathfrak{T}/\tau} + a\tau\mathfrak{T} - a\tau^2 \tag{3.23}$$

$$\delta n_i^{Second}(\mathfrak{T}) = \left[\delta n_i^{0,\ Second} - \frac{aT\tau}{4} - a\tau^2\right] e^{-(\mathfrak{T}-T/4)/\tau} - a\tau\left(\mathfrak{T} - T/2\right) + a\tau^2 \tag{3.24}$$

$$\delta n_i^{Third}(\mathfrak{T}) = \left[\delta n_i^{0,\ Third} + \frac{aT\tau}{4} + a\tau^2\right] e^{-(\mathfrak{T}-3T/4)/\tau} + a\tau\left(\mathfrak{T} - T\right) - a\tau^2, \tag{3.25}$$

that corresponds to the solution for the i^{th} voltage cycle, with the following initial conditions,

$$\delta n_i^{0,\ Second} = \delta n_i^{First}(\mathfrak{T} = T/4), \tag{3.26}$$

$$\delta n_i^{0,\ Third} = \delta n_i^{Third}(\mathfrak{T} = 3T/4). \tag{3.27}$$

Which yields, rewriting all the expressions in terms of the initial condition of the *First* region of the i^{th} cycle

$$\delta n_i^{First}(\mathfrak{T}) = \left[\delta n_i^{0,\ First} + a\tau^2\right] e^{-\mathfrak{T}/\tau} + a\tau\mathfrak{T} - a\tau^2 \tag{3.28}$$

$$\delta n_i^{Second}(\mathfrak{T}) = \left[\delta n_i^{0,\ First} + a\tau^2\right] e^{-\mathfrak{T}/\tau} - a\tau^2\left[2e^{-(\mathfrak{T}-T/4)/\tau} - 1\right] - a\tau\left(\mathfrak{T} - T/2\right) \tag{3.29}$$

$$\begin{aligned}\delta n_i^{Third}(\mathfrak{T}) = \left[\delta n_i^{0,\ First} + a\tau^2\right] e^{-\mathfrak{T}/\tau} - a\tau^2\left[2e^{-(\mathfrak{T}-T/4)/\tau} - 2e^{-(\mathfrak{T}-3T/4)\tau} + 1\right] \\ + a\tau\left(\mathfrak{T} - T\right)\end{aligned} \tag{3.30}$$

Now we can get a recursive relation for the initial condition of each cycle, realizing that the end of a i^{th}, using $\delta n^{Third}(\mathfrak{T})$, region should be equal to the beginning of the $(i+1)^{th}$ cycle, given by $\delta n^{First}(\mathfrak{T})$:

$$\delta n_{i+1}^{First}(\mathfrak{T} = 0) = \delta n_{i+1}^{0,\ First} = \delta n_i^{Third}(\mathfrak{T} = T), \tag{3.31}$$

which yields the following recursive form for the initial condition of the first set of equations:

$$n_{i+1}^{0,\ First} = \lambda + n_i^{0,\ First} e^{-T/\tau}, \tag{3.32}$$

where λ is can be written as:

$$\lambda \equiv a\tau^2\left[e^{-T/\tau} - 2e^{-3T/4\tau} + 2e^{-T/4\tau} - 1\right]. \tag{3.33}$$

Now, using the recursive form of Eq. 3.32 and starting at the $i = 0$, we have

$$\begin{aligned}
&\delta n_{i=0}^{0,First} \equiv \delta n_0^0 \\
&\delta n_{i=1}^{0,First} \equiv \delta n_1^0 = \lambda + \delta n_0^0 e^{-T/\tau} \\
&\delta n_{i=2}^{0,First} \equiv \delta n_2^0 = \lambda + \lambda e^{-T/\tau} + \delta n_0^0 e^{-2T/\tau} \\
&\delta n_{i=3}^{0,First} \equiv \delta n_3^0 = \lambda + \lambda e^{-T/\tau} + \lambda e^{-2T/\tau} + \delta n_0^0 e^{-3T/\tau} \\
&\ldots \\
&\delta n_{i=N}^{0,First} = \delta n_0^0 \cdot \left(e^{-T/\tau}\right)^N + \lambda \cdot \sum_{j=0}^{N-1}\left(e^{-T/\tau}\right)^j, \text{ for } i > 0.
\end{aligned} \tag{3.34}$$

And solving the geometric progression sum, we can write

$$\delta n_{i=N}^{0,First} \equiv \delta n_N^0 = n_{i=0}^{0,First}\, e^{-NT/\tau} + \lambda\, \frac{1-e^{-NT/\tau}}{1-e^{-T/\tau}}, \qquad i \equiv N \geq 0, \tag{3.35}$$

where we have denoted $\delta n_{i=N}^{0,First}$ in a more concise form, just as δn_N^0. In order to be clear, n_0^0 $(N=0)$ means that no complete cycle have been achieved yet, while δn_N^0 indicates that N complete cycles have been already achieved. So now, the Equations (3.28),(3.29),(3.30) that described a i^{th}-cycle in terms of the initial conditions of these i^{th}-cycles, can be rewritten in a more explicit way, in terms of the very initial condition, i.e. the condition for the $i=0$ cycle (δn_0^0), just using Eq (3.35) of δn_N^0:

$$\delta n_N^{I,Tri}(\mathfrak{T}) = \begin{cases} \left[\delta n_N^0 + a\tau^2\right] e^{-\mathfrak{T}/\tau} + a\tau\mathfrak{T} - a\tau^2 \\ \left[\delta n_N^0 + a\tau^2\right] e^{-\mathfrak{T}/\tau} - a\tau^2\left[2e^{-(\mathfrak{T}-T/4)/\tau} - 1\right] - a\tau\left(\mathfrak{T} - T/2\right) \\ \left[\delta n_N^0 + a\tau^2\right] e^{-\mathfrak{T}/\tau} - a\tau^2\left[2e^{-(\mathfrak{T}-T/4)/\tau} - 2e^{-(\mathfrak{T}-3T/4)\tau} + 1\right] \\ \qquad\qquad +a\tau\left(\mathfrak{T} - T\right) \end{cases}, \tag{3.36}$$

with $\mathfrak{T}$ belonging to the respective intervals: $\{\left[0, \frac{T}{4}\right],\ \left[\frac{T}{4}, \frac{3T}{4}\right],\ \left[\frac{3T}{4}, T\right]\}$.

For a sufficiently high number o cycles N, from Eq. (3.35), we can write the initial condition for stables cycles as:

$$n_\infty^{0,\,First} \equiv \lim_{N\to\infty} \delta n_N^{0,\,First} = \lambda \frac{1}{1-e^{-T/\tau}} \tag{3.37}$$

So, the stable cycle solution for $\delta n(\mathfrak{T})$ can be written as

$$\delta n_\infty^{I,Tri}(\mathfrak{T}) = \begin{cases} 2a\tau^2\left(\dfrac{1-e^{-T/2\tau}}{1-e^{-T/\tau}}\right) e^{-(\mathfrak{T}+T/4)/\tau} + a\tau\mathfrak{T} - a\tau^2, & 0 \leq \mathfrak{T} \leq \frac{T}{4} \\ 2a\tau^2\left(\dfrac{1-e^{-T/2\tau}}{1-e^{-T/\tau}}\right) e^{-(\mathfrak{T}+T/4)/\tau} & \\ \qquad -a\tau^2\left[2e^{-(\mathfrak{T}-T/4)/\tau} - 1\right] - a\tau\left(\mathfrak{T} - T/2\right), & \frac{T}{4} \leq \mathfrak{T} \leq \frac{3T}{4} \\ 2a\tau^2\left(\dfrac{1-e^{-T/2\tau}}{1-e^{-T/\tau}}\right) e^{-(\mathfrak{T}+T/4)/\tau} & \\ \qquad -a\tau^2\left[2e^{-(\mathfrak{T}-T/4)/\tau} - 2e^{-(\mathfrak{T}-3T/4)\tau} + 1\right] & \\ \qquad\qquad +a\tau\left(\mathfrak{T} - T\right), & \frac{3T}{4} \leq \mathfrak{T} \leq T. \end{cases} \tag{3.38}$$

The current of the system can then be calculated as

$$I_\infty^{I,Tri} = \left(G_0 + \alpha\, \delta n_\infty^{I,Tri}(\mathfrak{T})\right) V_{Triangular}(\mathfrak{T}), \tag{3.39}$$

while the conductance is just

$$G_\infty^{I,Tri} = G_0 + \alpha\, \delta n_\infty^{I,Tri}(\mathfrak{T}). \tag{3.40}$$

And the conductance values at $V_{Triangular} = 0$ are given by

$$G_{\infty,Low}(\mathfrak{T}=0) = G_0 - \alpha a \tau^2 \left[1 - 2\left(\frac{1-e^{-T/2\tau}}{1-e^{-T/\tau}}\right) e^{-T/4\tau}\right] \tag{3.41}$$

$$G_{\infty,High}(\mathfrak{T}=\frac{T}{2}) = G_0 + \alpha a \tau^2 \left[1 - 2\left(\frac{1-e^{-T/2\tau}}{1-e^{-T/\tau}}\right) e^{-T/4\tau}\right] \tag{3.42}$$

In turn, the *Content* values can also be calculated analytically

$$S_{up} = \int_{\mathfrak{T}=0}^{T/2} I(\mathfrak{T}) dV, \tag{3.43}$$

$$S_{down} = \int_{\mathfrak{T}=T/2}^{T} I(\mathfrak{T}) dV, \tag{3.44}$$

with $S_{up}^{Tri,I} = -S_{down}^{Tri,I}$, yielding

$$S_{up}^{Tri,I} = -\frac{4\, V_{max}^3\, \alpha\, \sigma_1 \tau^2}{T^3} \cdot \left[\frac{\left[\left(1+e^{T/2\tau}\right)\, T^2 - 8\left(-1+e^{T/2\tau}\right)\, T\, \tau + 32 \cdot \left(-1+e^{T/4\tau}\right)^2 \tau^2\right]}{e^{T/2\tau}+1}\right]. \tag{3.45}$$

This expression allows finding numerically the optimal period to maximize content in absolute values as being

$$T_{\max}^{Tri,I} \approx 6.754957\, \tau. \tag{3.46}$$

Note that the maximum area for the corresponding system with a sinusoidal voltage was, $T_{\text{Sin max}} = 2\pi\tau \approx 6.2831\tau$.

3.2.2 Type-II System

In this case, we look for the solutions of

$$\frac{d\delta n(t)}{dt} = -\frac{\delta n(t)}{\tau} + \sigma_2 V_{Tri}^{(II)}, \tag{3.47}$$

with $V_{Tri}^{(II)}$ given by Eq. (3.17) and we will split the solution in two different regions, that we call

$$First \equiv \left\{\mathfrak{T},\ \mathfrak{T} \in \left[0, \frac{T}{4}\right]\right\}, \tag{3.48}$$

$$Second \equiv \left\{\mathfrak{T},\ \mathfrak{T} \in \left[\frac{T}{4}, \frac{T}{2}\right]\right\}, \tag{3.49}$$

with $\mathfrak{T}$ being the effective time inside each semi cycle i, i.e. $t \equiv (i-1)\frac{T}{2} + \mathfrak{T}$. Now, in a similar manner, lets define a useful constant

$$a_2 \equiv \frac{4\sigma_2 V_0}{T}, \tag{3.50}$$

thus, for the corresponding time intervals, we have

$$\delta n_i^{First}(\mathfrak{T}) = \left[\delta n_i^{0,\ First} + a\tau^2\right] e^{-\mathfrak{T}/\tau} + a\tau\mathfrak{T} - a\tau^2, \tag{3.51}$$

$$\delta n_i^{Second}(\mathfrak{T}) = \left[\delta n_i^{0,\ Second} - \frac{aT\tau}{4} - a\tau^2\right] e^{-(\mathfrak{T}-T/4)/\tau} - a\tau\left(\mathfrak{T} - T/2\right) + a\tau^2, \tag{3.52}$$

with,

$$\delta n_i^{0,\ \mathrm{Second}} = \delta n_i^{First}(\mathfrak{T} = T/4) = \left[n_i^{0,\ First} + a\tau^2\right] e^{-T/4\tau} + a\tau\frac{T}{4} - a\tau^2, \tag{3.53}$$

where the index i is now counting *semi-periods* of the voltage cycles, starting at $i = 1$ for the very first cycle.[2] Now in order to obtain a relation for the initial condition of each cycle, note that

$$\delta n_{i+1}^{0,\ First} = \delta n_i^{Second}(\mathfrak{T} = T/2) \qquad , \text{ for } i \geq 1, \tag{3.54}$$

yielding

$$n_{i+1}^{0,\ First} = \lambda + n_i^{0,\ First} e^{-T/2\tau}, \tag{3.55}$$

$$\text{with, } \lambda \equiv a\tau^2\left[1 - 2e^{-T/4\tau} + e^{-T/2\tau}\right] = a\tau^2\left(1 - e^{-T/4\tau}\right)^2. \tag{3.56}$$

This recursive relation can be rewritten in a more detailed form (term by term) just like we did in Eq. (3.34). And in a similar fashion, we can write the N^{th}-half cycle initial condition *(of the first half interval)* in terms of the initial condition of the first half-cycle and of a sum of a geometric progression, as

$$n_{i=N}^{0,\ First} = \lambda\left[\sum_{j=1}^{N-1}\left(e^{-T/2\tau}\right)^{j-1}\right] + n_{i=1}^{0,\ First}\left(e^{-T/2\tau}\right)^{N-1}, \tag{3.57}$$

for $i = N \geq 2$; while for $N = 1$ (the very first half cycle) we have $n_{i=1}^{0,First} \equiv n_0^0$.[3] The sum of this geometric progression, with initial term $a_1 = \lambda$ and ratio $q = e^{-T/2\tau}$ can be evaluated, yielding

$$\delta n_{i=N}^{0,\ \mathrm{First}} \equiv \delta n_N^0 = \lambda\left(\frac{1 - e^{-(T/2\tau)(N-1)}}{1 - e^{-T/2\tau}}\right) + \delta n_{i=1}^{0,\ First} e^{-(T/2\tau)(N-1)}, \quad \text{for } N \geq 1, \tag{3.58}$$

with N counting half-cycles, starting at $N = 1$.

For a sufficiently high number of half-cycles N, we can get the initial condition of the stables half-cycles, as

$$n_\infty^{0,\ First} \equiv \lim_{N\to\infty} \delta n_N^{0,\ First} = \lambda\frac{e^{T/2\tau}}{e^{T/2\tau} - 1}. \tag{3.59}$$

[2] It is worth noting that here, in triangular Type-II system the counting index i is starting at *i=1* for the first count piece and is counting voltage *semi-cycles*; while, for the previous triangular Type-I system, the index i starts its counting at *i=0*, and counts *entire* voltage cycles

[3] Where i or N here ($i \equiv N$) corresponds to a counting index of the *half-cycles* and not of the entire voltage cycles.

So we can write the solution of the stable half-cycles in the following manner

$$\delta n_{\infty}^{II,Tri}(\mathfrak{T}) = \begin{cases} a\tau^2\left\{e^{-\mathfrak{T}/\tau}\left[coth(\frac{T}{4\tau}) - csch(\frac{T}{4\tau}) + 1\right] - 1\right\} + \frac{a}{\tau}\mathfrak{T}, & 0 \le \mathfrak{T} \le \frac{T}{4} \\ a\tau^2\{e^{-(\mathfrak{T}-T/2)/\tau}\left[coth(\frac{T}{4\tau}) - csch(\frac{T}{4\tau}) + 1\right] - 1\} & \\ \qquad -\frac{a}{\tau}(\mathfrak{T} - \frac{T}{2}), & \frac{T}{4} \le \mathfrak{T} \le \frac{T}{2}. \end{cases} \tag{3.60}$$

Now, we make a short break in our logical reasoning before describing the current, in order to define useful asymptotic expressions that will be suited to evaluate important expressions later on. For simplicity, lets define the $H_Y(x)$ function as:

$$H_Y(x) \equiv \coth(x) - \operatorname{csch}(x). \tag{3.61}$$

Considering $H_Y(x)$ it is worth noting its asymptotic limits and its first order Taylor expansion form, respectively [4]

$$\lim_{x\to\infty} H_Y(x) = 1, \tag{3.62}$$

$$\lim_{x\to 0} H_Y(x) = 0, \tag{3.63}$$

$$H_Y(x) \cong \frac{x}{2}, \tag{3.64}$$

where the third one is valid for sufficiently small arguments (x), until its first order.

By applying Eq. (3.62), Eq. (3.63) and Eq. (3.64) to Eq. (3.60), of $\delta n_{\infty}^{II,Tri}$, we obtain the following asymptotic forms in period for $\delta n_{\infty}^{II,Tri}(\mathfrak{T})$:

$$\lim_{T\to 0} \delta n_{\infty}^{II,Tri}(\mathfrak{T}) = \frac{\sigma_2 V_0 \tau}{2} \tag{3.65}$$

$$\lim_{T\to\infty} \delta n_{\infty}^{II,Tri}(\mathfrak{T}) = \begin{cases} V_0\sigma_2\tau 4\,\chi, \text{ for } \mathfrak{T} \le T/4;\ \chi \in [0, 1/4], \text{ with } \mathfrak{T} \equiv \chi T \\ V_0\sigma_2\tau[1 - 4\,\chi], \text{ for } \mathfrak{T} \ge T/4;\ \chi \in [0, 1/4], \text{ with } \mathfrak{T} \equiv \frac{T}{4} + \chi T \end{cases} \tag{3.66}$$

Now, once the useful limits of $\delta n_{\infty}^{II,Tri}(period)$ have been established, lets return to the physics and define the current of the system as

$$I_{\infty}^{II,Tri} = \left(G_0 + \alpha\,\delta n_{\infty}^{II,Tri}(\mathfrak{T})\right) \cdot V_{Triangular}(\mathfrak{T}), \tag{3.67}$$

while the conductance is just given by

$$G_{\infty}^{II,Tri}(\mathfrak{T}) = G_0 + \alpha\,\delta n_{\infty}^{II,Tri}(\mathfrak{T}). \tag{3.68}$$

Now, calculating the zero point conductance (at $V_{Triangular}(\mathfrak{T}) = 0$) for the beginning and the end of the first and second half-cycles, respectively, we have [5]

$$\begin{aligned} G_{\infty}^{i}(\mathfrak{T} = 0) &= G_{\infty}^{i+1}(\mathfrak{T} = T/2) \\ &= G_0 + \alpha\left\{\left(\frac{8\sigma_2 V_0 \tau^2}{T}\right)\cdot\left[\frac{e^{T/4\tau} - 1}{e^{T/2\tau} - 1}\right]\cdot e^{T/4\tau} - \frac{4\sigma_2 V_0}{T}\tau^2\right\} \end{aligned} \tag{3.69}$$

[4] These expressions will be used later on in this text.

[5] Which means, the values at the start and the end of a entire cycle, i.e. of two sequential half-cycles.

which reinforces this system as a Type-II (symmetric type).

We can also calculate the asymptotic forms of the zero-conductance as a function of period by using the δn limits, given by Eq. (3.65) and Eq. (3.66), and replacing them in the conductance Eq. (3.68) while setting $\mathfrak{T} = 0$, which yields

$$\lim_{T\to\infty} G_{\infty}^{II,Tri}\left(\mathfrak{T}=0\right) = G_0, \tag{3.70}$$

$$\lim_{T\to 0} G_{\infty}^{II,Tri}\left(\mathfrak{T}=0\right) = G_0 + \frac{\alpha\sigma_2 V_0 \tau}{2}. \tag{3.71}$$

The *Content* values will be defined as

$$S_{up} = \int_{\mathfrak{T}=0}^{T/2} I(\mathfrak{T}) dV_{Triangular} \tag{3.72}$$

$$S_{down} = \int_{\mathfrak{T}=T/2}^{T} I(\mathfrak{T}) dV_{Triangular} = S_{up} \tag{3.73}$$

Specifically, for the upper loop we can write

$$S_{up} = \int_{\mathfrak{T}=0}^{T/4} I(\mathfrak{T}) dV + \int_{\mathfrak{T}=T/4}^{T/2} I(\mathfrak{T}) dV, \tag{3.74}$$

that is

$$\begin{aligned} S_{up} = &\int_{\mathfrak{T}=0}^{T/4} (G_0 + \alpha\, \delta n_{\infty}^{II,Tri}(\mathfrak{T})) \left(\frac{4V_0}{T}\,\mathfrak{T}\right)\left(\frac{4V_0}{T}\right) d\mathfrak{T} + \\ &\int_{\mathfrak{T}=T/4}^{T/2} (G_0 + \alpha\, \delta n_{\infty}^{II,Tri}(\mathfrak{T})) \left(2V_0 - \frac{4V_0}{T}\mathfrak{T}\right)\left(-\frac{4V_0}{T}\mathfrak{T}\right) d\mathfrak{T}. \end{aligned} \tag{3.75}$$

Yielding the following explicit formulae for the contents (considering the Type-II symmetric response of this system):

$$\begin{aligned} &S_{up} = S_{down} = 64\alpha\sigma_2 V_{max}^3 \frac{\tau^2}{T^3} \\ &\left\{2\tau^2 - [H_Y(T/4\tau)+1]\left(\tau^2 + \frac{T}{4}\tau\right)e^{-T/4\tau} + [H_Y(T/4\tau)-1]\left(\tau^2 - \frac{T}{4}\tau\right)e^{T/4\tau} - \frac{T^2}{16}\right\} \end{aligned} \tag{3.76}$$

Now, by introducing the parameter $x \equiv T/4\tau$, the expression in Eq. (3.76) can be rewritten equivalently in a simpler way, as

$$S_{up} = S_{down} = \alpha\,\sigma_2\, V_0^3\, \tau \left\{\frac{2}{x^2}\left(\frac{e^x - 1}{e^x + 1}\right) - \frac{1}{x}\right\}. \tag{3.77}$$

This can be used to find numerically the optimal period capable of maximizing the content in absolute values, that is

$$T_{max}^{II,Tri} \approx 12.8489\,\tau\ , \tag{3.78}$$

Note that the maximum for the corresponding system with a sinusoidal voltage was achieved for: $T_{\mathrm{Sin,max}} = 4\pi\tau \approx 12.5664\,\tau$

3.2.2.1 Comparing the Triangular Systems's Responses

From the equations Eq. (3.36) (for a type-I system); and Eq.(3.51), Eq.(3.52) (for a type-II system), we can compare the evolution of their non-equilibrium carriers, $\delta n^{I,II}$, in time. As depicted in Fig. (11).

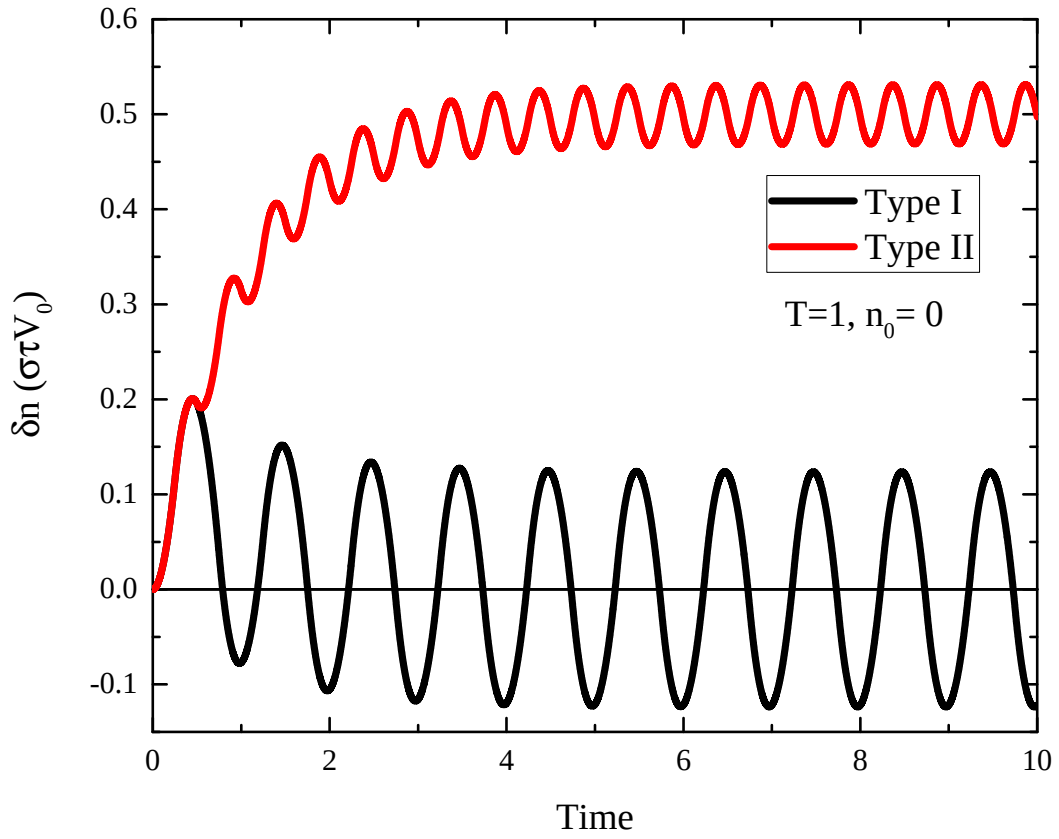

Figure 11 – Transient behaviour of δn^I and δn^{II}. Parameters are: $\sigma_1 = \sigma_2 = 100$; $\tau = 1$; $T = 10$; $V_0 = 1; n_0 = 0$; $G_0 = 1$; $\alpha = 0.01$. After a sufficiently long time the systems reach the stable regimes.

We can also compare the behavior of the systems, in their stable regimes, looking at their currents in a time interval of a single voltage cycle, as depicted in Fig (12).

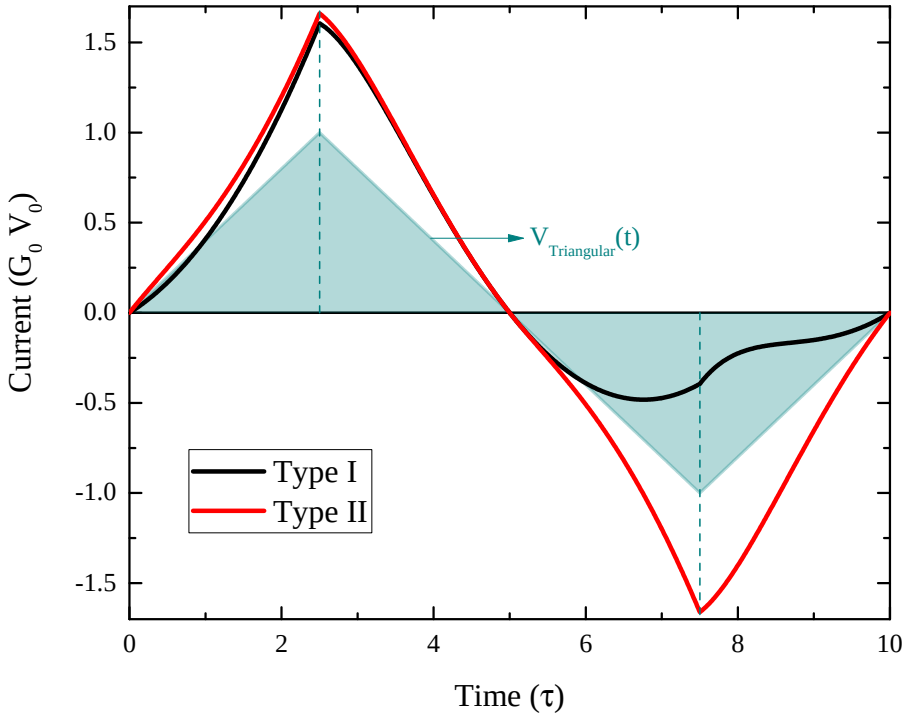

Figure 12 – Normalized currents and voltage for one stable cycle. Parameters are: $\sigma_1 = \sigma_2 = 100$; $\tau = 1$; $T = 10$; $V_0 = 1; n_0 = 200$; $G_0 = 1$; $\alpha = 0.01$.

Note that the discontinuity in the first derivative of the voltage input (at $\mathfrak{T} = T/4$ and $\mathfrak{T} = 3T/4$) leads to discontinuities in both currents derivatives.

From the equations of current, namely, Eq. (3.39) for Type-I; and Eq. (3.67) for Type-II; we can compare their I-V characteristics, as depicted in Fig. 13.

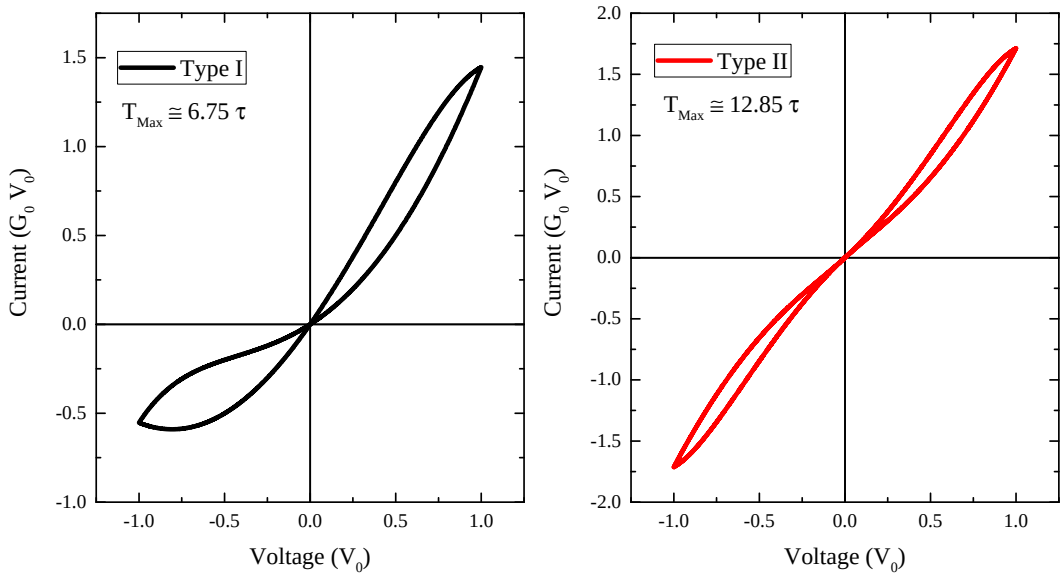

Figure 13 – Current voltage curves for a) Type I system, with maximum in $T = 6.75\,\tau$; and type II, with maximum in $T = 12.85\,\tau$, b).Parameters are: $\sigma_1 = \sigma_2 = 100$; $\tau = 1$; $V_0 = 1; n_0 = 200$; $G_0 = 1$; $\alpha = 0.01$.

Note also that the period, T, of them is different in these plots, and have been

chosen in order to maximize the content values of their hysteresis; i.e., for the Type-I system we have $T^{I}_{Max} \approx 6.75\,\tau$, while $T^{II}_{Max} \approx 12.85\,\tau$, for Type-II.

From Eqs. (3.40) and (3.68) we can plot figures of merit of the conductance of the systems as a function of voltage ($V_{Triangular}$), as displayed in Fig. 14.

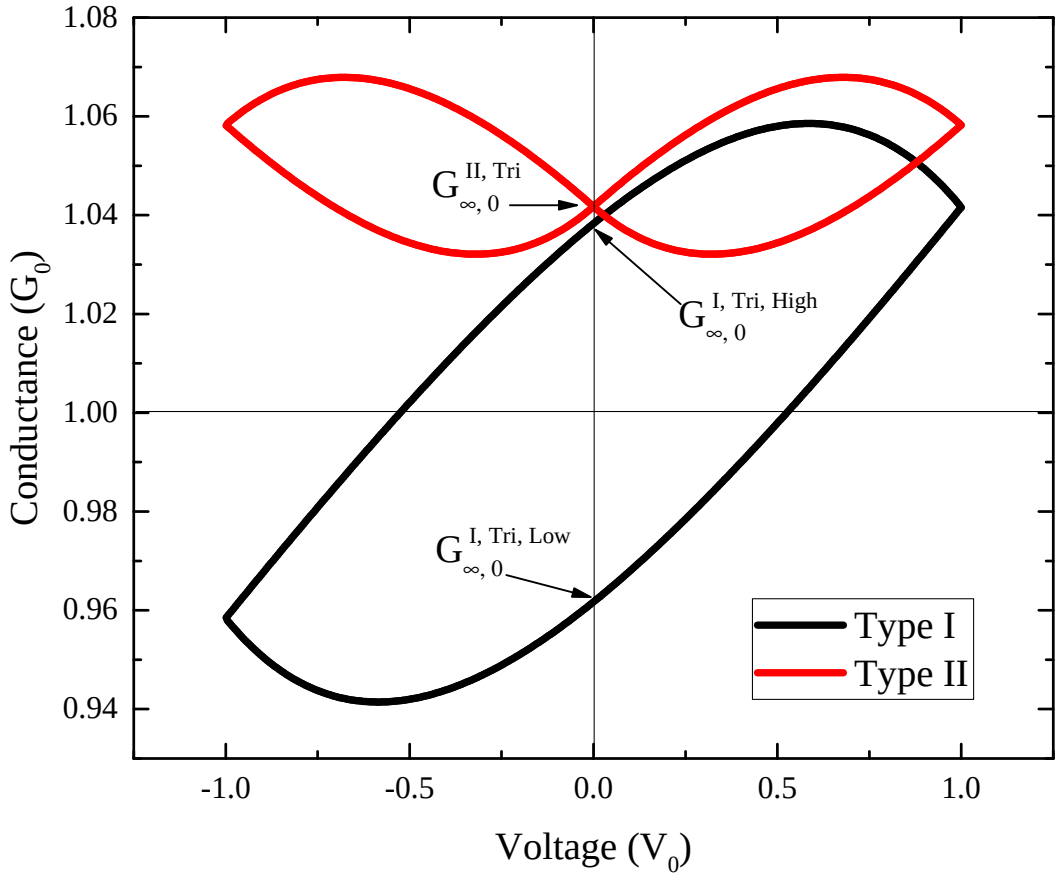

Figure 14 – Normalized conductance as a function of voltage for a stable cycle. The Type-I system presents two conductance states at zero voltage, high and low, while Type-II, the symmetric one, present only one state. The parameters used are: $\sigma_1 = \sigma_2 = 100$; $\tau = 1$; $V_0 = 1$; $n_0 = 100$; $G_0 = 1$; $\alpha = 0.001$ and $T = 2\pi$.

The discontinuities of the conductance derivatives at extreme left and right positions are expected because of the discontinuities on the voltage's derivative function $\left(\frac{d}{d\mathfrak{T}} V_{Triangular}(\mathfrak{T})\right)$ at these same positions. Also, at zero voltage, the Type-I system presents two different conduction states (*High* and *Low*) while Type-II presents a unique conduction state, just like for the sinusoidal voltage input.

The conductance states at zero voltage are written in Eqs. (3.41, 3.42) for the Type-I system and in Eq. (3.69), for the Type-II. These equations can rewritten in the

following normalized form

$$\frac{G^{I,Tri,Low}_{\infty,V=0} - G_0}{\sigma_1 \alpha \tau V_0} = -4\left(\frac{\tau}{T}\right)\left[1 - 2\left(\frac{1-e^{-T/2\tau}}{1-e^{-T/\tau}}\right)e^{-T/4\tau}\right] \tag{3.79}$$

$$\frac{G^{I,Tri,High}_{\infty,V=0} - G_0}{\sigma_1 \alpha \tau V_0} = +4\left(\frac{\tau}{T}\right)\left[1 - 2\left(\frac{1-e^{-T/2\tau}}{1-e^{-T/\tau}}\right)e^{-T/4\tau}\right] \tag{3.80}$$

$$\frac{G^{II,Tri}_{\infty,V=0} - G_0}{\sigma_2 \alpha \tau V_0} = 8\left(\frac{\tau}{T}\right)\left[\frac{\mathrm{Exp}\left(\frac{1}{4}\frac{T}{\tau}\right) - 1}{\mathrm{Exp}\left(\frac{1}{2}\frac{T}{\tau}\right) - 1}\right] \cdot \mathrm{Exp}\left(\frac{1}{4}\frac{T}{\tau}\right) - 4\left(\frac{\tau}{T}\right) \tag{3.81}$$

The normalized states of conductance at zero voltage, as a function of the period, from Eqs. (3.79, 3.80, 3.81), are shown in Fig. 15.

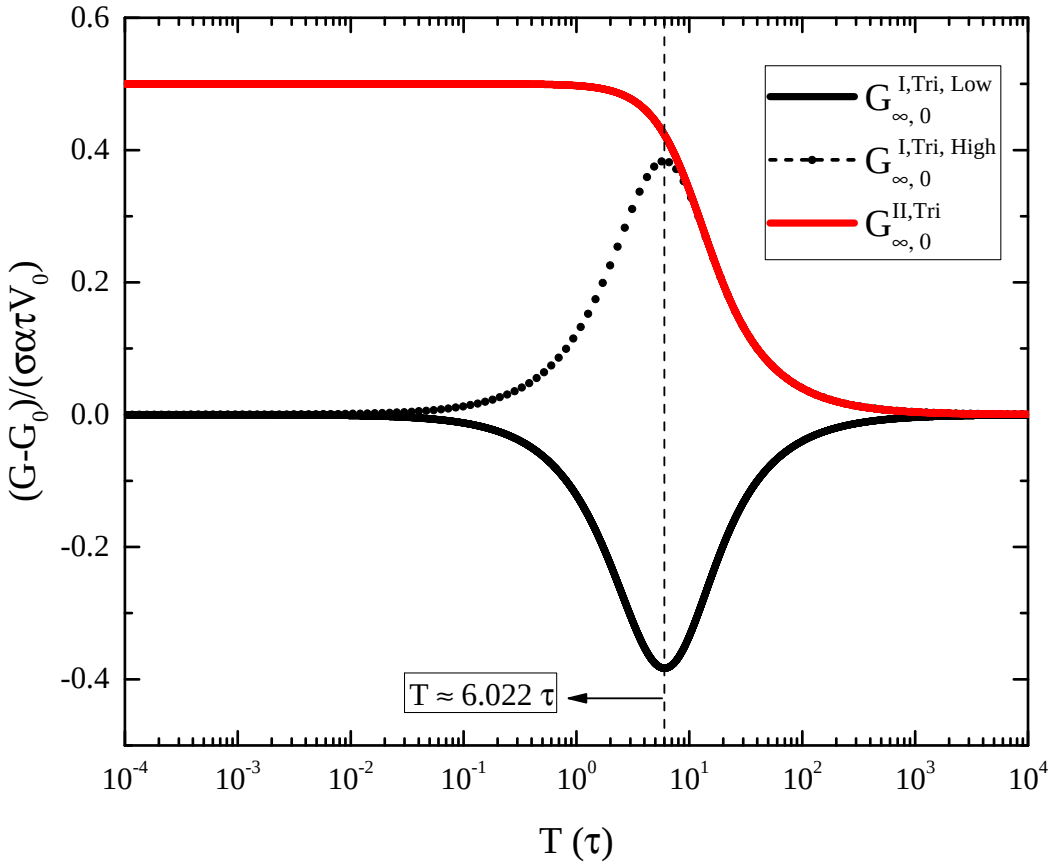

Figure 15 – Normalized difference of the zero-conductance states with their unperturbed conductance (G_0) as functions of the period (T). The two different conductances states of Type-I system are depicted in black: the dotted line for the higher state and continuous one, for the lower. Also, the maximum difference between these states is achieved at the period $T \approx 6.022\,\tau$ (obtained numerically). The unique conduction state of the Type-II system is depicted in the red continuous line and their asymptotic values are in perfect agreement with the equations 3.70 and 3.71. Parameters are: $\sigma_1 = \sigma_2 = 100$; $\tau = 1$; $V_0 = 1; n_0 = 100$; $G_0 = 1$; $\alpha = 0.001$.

It can be seen, in Fig. (15) , that for high values of period, i.e. very small values of the frequency $\omega \equiv T/2\pi$, all the conductance states (for both systems) converge to their unperturbed value (G_0). This phenomenon is expected and can be understood considering

that the input voltage function changes so slow, that the system has enough time to return to the unperturbed state, by means of the relaxation time (τ) mechanism.[6]

For small values of T, i.e. high frequencies ω, the Type-I system still returns to its unperturbed state (G_0) due to the oscillating character between negative and positive values of voltage of its generation function. In contrast, the Type-II system reaches a kind of stable conductance state that is different from (G_0) and it can be understood if we note that its generation function dependence with voltage is oscillating very fast but *only in positive values of voltage*. Thus, we have a kind of either fast excitation or trapping mechanism (and not both) and also a relaxation mechanism (driven by τ). Therefore, the interplay between the very fast generation mechanism and the relaxation one reaches a steady equilibrium, yielding a conductance value different from (G_0).

The normalized upper content values of Eq. (3.45), for Type-I system, and Eq. (3.76), for Type-II are depicted in Fig. (16).

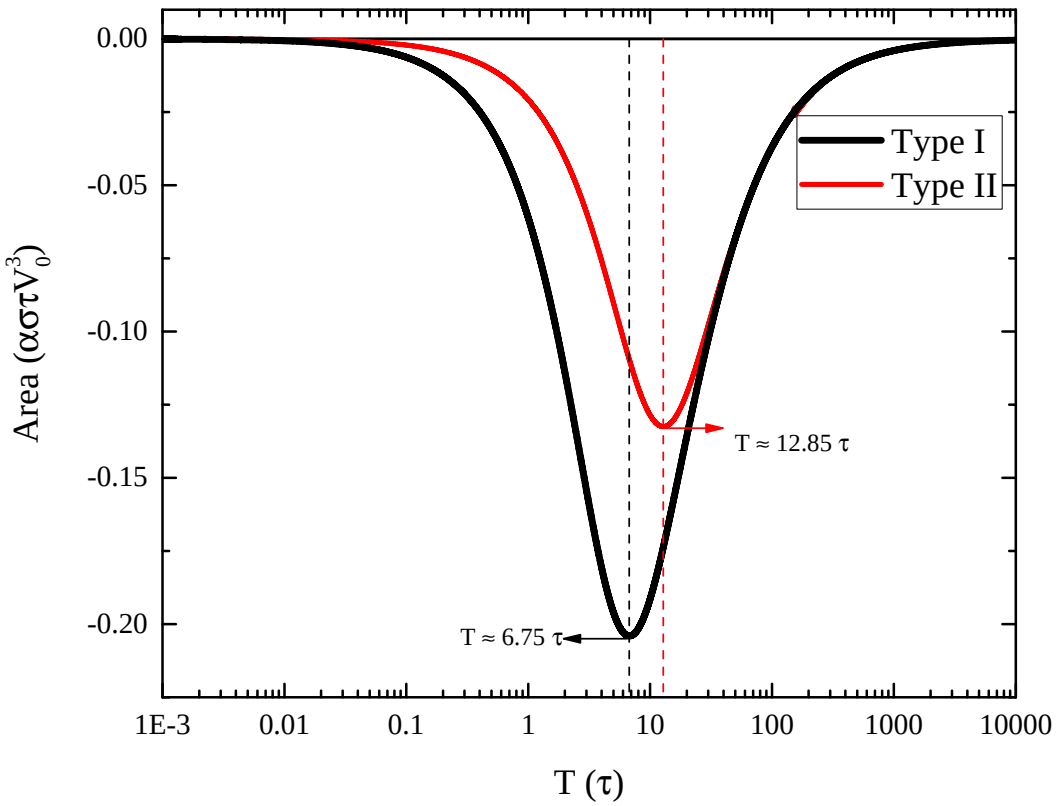

Figure 16 – Normalized content values for the upper loops of Type-I and (II) systems. The Type-I, black curve, presents a higher absolute value of content with a maximum at $T \approx 6.75\,\tau$; while the Type-II system, in red, presents its maximum at $T \approx 12.85\,\tau$. Parameters are: $\sigma_1 = \sigma_2 = 100$; $\tau = 1$; $V_0 = 1; n_0 = 100$; $G_0 = 1$; $\alpha = 0.001$.

It can be seen that, just like for the sinusoidal input, the triangular pulse induces the Type-I system to reach a maximum absolute content value greater than the corresponding one for Type-II case. Also, the Type-I maximum content is attained at lower values of

[6] See the differential equations Eq. (3.18) and Eq. (3.47).

period (i.e. greater values of frequency), compared to Type-II, just like for the sinusoidal responses. The exact position of the maximum values were obtained numerically from the equations Eq. (3.45) and Eq. (3.76).

3.3 Optimizing the Systems

In order to summarize how to tune the systems to their optimal regime of operation of *content* and displacement between the conductive states *High* and *Low* (of Type-I system), we present Table 1 .

Table 1 – Tuning values of period in units of τ in order to maximze the memory response of the *toy models*, regarding the content and the displacement between *High* and *Low* conductivit states of Type-I systems.

	$\boldsymbol{\Delta\sigma^{I}_{max}}$**displacement - position**	$\boldsymbol{Area_{max}}$**Position**
Type-I Sinusoidal	$2\pi\tau \approx 6.283\,\tau$	$2\pi\tau \approx 6.283\,\tau$
Type-II Sinusoidal	- - -	$4\pi\tau \approx 12.57\,\tau$
Type-I Triangular	$\approx 6.022\,\tau$	$\approx 6.75\,\tau$
Type-II Triangular	- - -	$\approx 12.58\,\tau$

4 Experimental confirmations and the effect of temperature in ZnO thin films

In this chapter we will use the model to explain and predict memory features that have emerged in samples of ZnO thin films fabricated and characterized by colleagues. These samples were subjected to triangular voltage pulses and the generating function that have been used here is that of Eq. 2.41, capable of modelling the carrier activation in *metal-semiconductor-metal* sites or *vice-versa*. Thus, as the generation function applied in this model is different of those used in the previous Chapter, it is expected that the conduction model applied here to be slightly different from that ones.

4.1 The Model for Metal-Semiconductor-Metal Sites

Beside internal parameters, the memristive response is also affected both qualitatively and quantitatively by the shape of the voltage drive. In this section we have modeled the system for triangular voltage pulses responses as displayed in the inset of Fig. 17, that is discussed alongside the experimental results in what follows. If the local voltage efficiency, η, is sufficiently low, then it is valid to assume that $\frac{\eta eV}{2k_BT_{eff}} << 1$ and Eq. (2.41) can be approximated up to second order in voltage reducing Eq. (2.37) to

$$\frac{d\delta n}{dt} = \frac{i_0\eta}{4}\left(\frac{eV}{k_BT_{eff}}\right)^2 - \frac{\delta n(t)}{\tau}. \tag{4.1}$$

Assuming the presence of just a single channel of n-type carriers, the solution of Eq. (4.1) under stationary conditions yields, $n^e_{st} = \frac{\pi m^*_e \eta \tau^e}{(2\pi\hbar)^3}(eV)^2 \exp\left(-\frac{E^e_B}{k_BT_{eff}}\right)$, that corresponds to activated electrons above a barrier E^e_B, where the subscript and superscripts (e) were introduced to label electron related parameters. The conductance at $V = 0$ can be emulated for the upward and downward sweeps under stable conditions, corresponding to coincident conductance values at $V = 0$ a typical feature of Type-II systems

$$G(0) = G\left(\frac{T}{2}\right) = G_0 + \frac{\alpha L}{1 - \exp\left(-\frac{T}{2\tau}\right)}, \tag{4.2}$$

with $L = 2\lambda\tau^3\left[1 - \exp\left(-\frac{T}{2\tau}\right)\right] - \lambda\tau^2 T\exp\left(-\frac{T}{4\tau}\right)$, and $\lambda = \frac{4\eta i_0}{T^2}(\frac{eV_0}{k_BT_{eff}})^2$. From Eq. (3.12), the *Content* can be obtained as

$$S_{\text{triangular}} = -\frac{\alpha 128\eta e^2 V_0^4 i_0 \tau}{(k_BT_{eff})^2}\left(\frac{\tau}{T}\right)^3 \frac{1 - e^{-\frac{T}{2\tau}}\left[\frac{1}{3}(\frac{T}{4\tau})^2 + \frac{T}{4\tau} + 1\right] + \frac{1}{3}(\frac{T}{4\tau})^2 - \frac{T}{4\tau}}{1 - e^{-\frac{T}{2\tau}}}, \tag{4.3}$$

with the corresponding analogue for a sinusoidal voltage pulse, written using the same parameter's notation of triangular response formalism, being written as

$$S_{\text{sinusoidal}} = -\frac{\alpha 128\eta e^2 V_0^4 i_0 \tau}{(k_B T_{eff})^2}\left(\frac{\pi}{1024}\right)\frac{\left(\frac{2\pi\tau}{T}\right)}{1+\left(\frac{4\pi\tau}{T}\right)^2}. \tag{4.4}$$

From the expressions above, it can be demonstrated that, in the case of the approximation of Eq. 4.1, the maximum absolute value of *Content* takes place at $T/\tau \approx 13.7434$ for triangular pulses while at $T/\tau = 4\pi$ for sinusoidal pulses.

4.2 The experiment

Increasing temperatures can be, in general, detrimental for memory functionalities. [32] However, as discussed in this section, combining experimental and theoretical analyses we concluded that this is not always true. In particular, the lateral transport in thin films of zinc oxide tends to have its memory character increased with the temperature rise. [26]

Thus, in this section, we discuss a practical example where the theory can be applied to explain and predict several features concerning the memory emergence and also how temperature affects it. A schematic diagram of this system can be seen in Fig. 17 (a), where the *texture* on the film surface represents the presence of defects, that can act as generation or trapping sites for conductive carriers; while in Fig 17 (b) the pattern of the triangular voltage input has been represented. This results in the measured hysteresis in Current-Voltage characteristics as displayed in Fig 17 (b).

Hall effect measurements were performed in a temperature range of $240K$ to $380K$, revealing an increase of n-type carriers at lower temperatures followed by a subsequent growth of the presence of holes, culminating in the reversal of the n-type behavior in favor of p-type transport, at higher temperatures, as can be seen in Fig. 17 (c). During the Hall effect measurements, the applied bias voltage changed, as depicted in Fig 17 (d), that shows the experimental voltage points and a fitting function. Using this fitting, the theoretically predicted carrier density as a function of temperature was plotted as a solid green line in Fig 17 (c), in good agreement with the experimental measurements, represented as green spheres. This observed interplay between carrier of different types as temperature changed pointed out to the need of modelling the system considering two independent conduction channels within this temperature range: one for electrons and another one for holes.

The dynamic Eq. 4.1 was used to model each channel, implying in a total number of non-equilibrium carriers (considering both contributions) proportional to

$$q_{\text{total}} \propto (eV)^2\left[\frac{m_h^*\tau^h}{m_e^*\tau^e}e^{-\frac{E_B^h}{k_B T_{eff}}} - e^{-\frac{E_B^e}{k_B T_{eff}}}\right]. \tag{4.5}$$

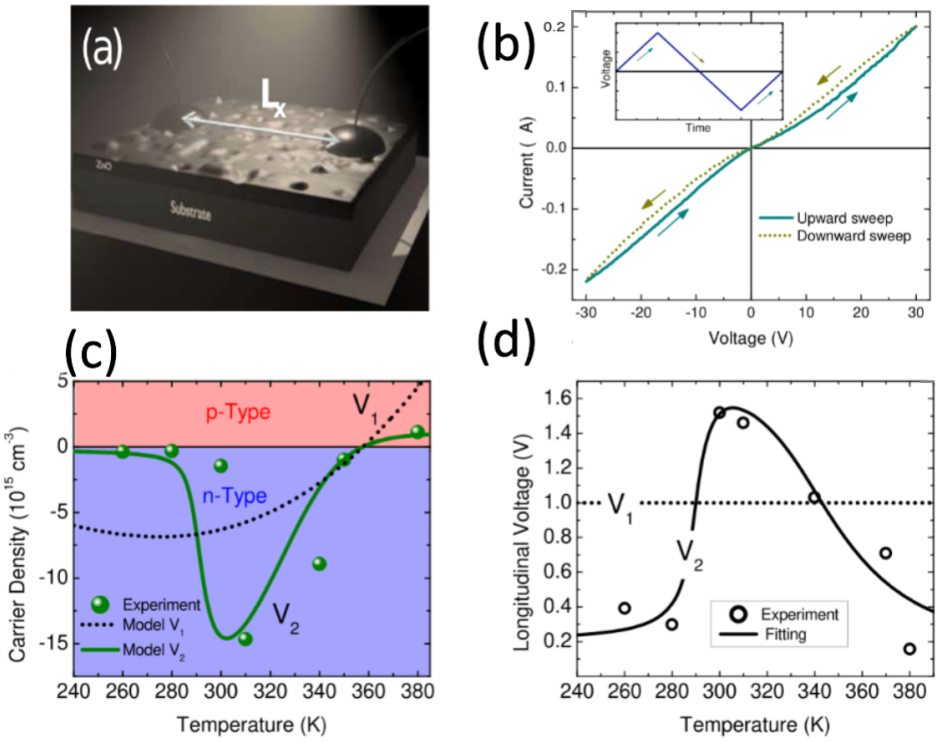

Figure 17 – (a) Schematic representation of the sample with contacts. (b) Measured current-voltage loop with the corresponding triangular voltage drive plotted in the inset. (c) Charge density as a function of temperature. (d) Applied longitudinal voltage for each temperature to set the fixed current condition.

Then, from the number of carriers, we theoretically obtained the zero voltage conductance values for half-period and full-period, which are given by Eq. (4.2), pointing out to a Type-II response, as they were found to be equal.

The loop area, over a whole cycle, was extracted from the stable experimental condition and is shown in Fig. 18 (a), with the theoretically calculated total area of Eq. 4.3, represented in Fig. 18 (b) that coincides with this functional behavior. The theoretical value of the hysteresis area collapses at both $T/\tau \to 0$ and $T/\tau \to \infty$, with a maximum absolute value at $T/\tau \approx 13.7434$ and given that the maximum experimental absolute loop area has been reached for $T = 120min$, we can estimate the corresponding relaxation time as being $\tau = 8.73$ min. A comparison between the behavior predicted for a triangular pulse and the corresponding analogue for the sinusoidal voltage input has also been included into Fig. 18 (b), pointing to similar functional behaviour but different values for the period that leads to the the maximum area.

Using the definition, $I = (G_0 + \alpha\,\delta n)V$, we can also find a theoretical expression for the zero voltage resistance taking into account the two active channels with electrons and holes contributions

$$R_{xx}^{m} = \left[G_0 + \gamma \left(\frac{m_h^* \tau^h}{m_e^* \tau^e} e^{-\frac{E_B^h}{k_B T_{eff}}} + e^{-\frac{E_B^e}{k_B T_{eff}}} \right) \right]^{-1}, \tag{4.6}$$

where γ is a constant value. This theoretical temperature dependence has been included

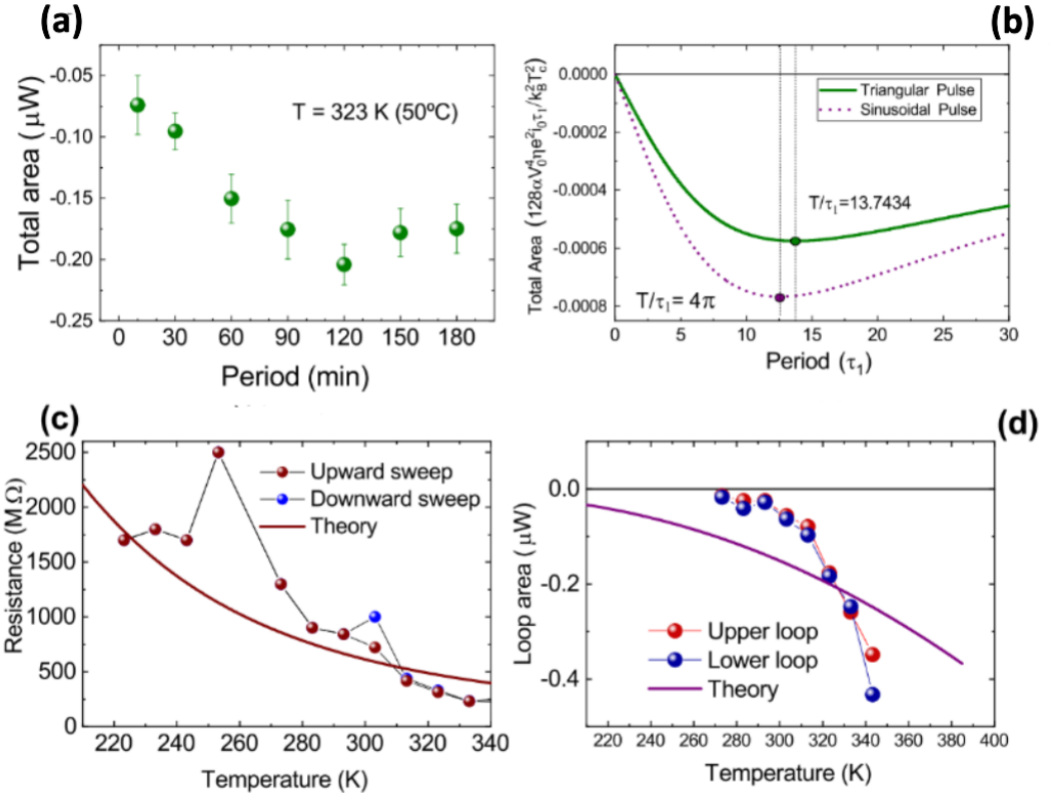

Figure 18 – (a) Measured total area of the current-voltage loop as a function of period. (b) Calculated total area of the current-voltage loop as a function of period for a triangular and a sinusoidal pulses. (c) Resistance at V = 0 as function of temperature. (d) Upper and lower loops areas as function of temperature.

into Fig. 18 (c) alongside the experimental measurements of the resistance. The agreement between these experimental and theoretical findings indicates that within this temperature frame it is the charge activation that rules the memory response.

The measurement of upper and lower *Content* and the precise match of them, as displayed in Fig. 18 (d) reinforces the previous assertion on the preservation of the Type-II character of the memristive response. The experiments also showed a decrease (increase in absolute values) in the *Content* value with the temperature rise, alongside the theoretical results as depicted in Fig 18 (d). The theoretical *Content Value* is obtained from Eq. 4.3, from which we can prove that $Content \propto -m\tau \exp[-E_B/(k_B T_{eff})]$, so that the temperature tuning of the area of a single loop, $A/2$, combining additive electron and hole channels, can be reduced to

$$A/2 \propto -\left(\frac{m_h^* \tau^h}{m_e^* \tau^e} e^{-\frac{E_B^h}{k_B T_{eff}}} + e^{-\frac{E_B^e}{k_B T_{eff}}}\right). \tag{4.7}$$

This theoretical function, is plotted alongside the experimental findings in Fig. 18 (d), and also defines a monotonic growth in absolute terms, in agreement with the experiments and reinforcing the dominance of charge activation in boosting these memory traces. Such a picture is expected to be reversed at much higher temperatures if the decay time, τ, so

far assumed to be independent on T_{eff}, decreases. Yet, this limit was clearly not reached within the temperature range of the current analysis.

5 Conclusion and next steps

Based on the results available thus far, we may conclude that this research into the memristive response in solids has already been very fruitful. From the outcome of our investigation it has been possible to model and emulate a pervasive mechanism of memory emergence in conductive solids, yielding both Type-I and Type-II responses according to certain symmetry constrains. One may also foresee further success in the application of our model to various systems and devices.

We have obtained analytical expressions that describe systems driven by a sinusoidal and triangular bias voltage, with linear antisymmetric generation rate and also for a symmetrical generation rate. We have presented analytical expressions for he current as a function of time, for both types of systems, and also for their conductance and *Content*. These results indicate how the memory response of these systems could be tuned by adjusting the bias frequency, amplitude, and temperature. Preliminary discussions on this matter were published in the paper *The Ubiquitous Memristive Response in Solids* [1]. We have also obtained experimental confirmations for the model validity employing the triangular voltage pulse formalism, [1] which were published in the paper *Temperature, detriment or advantage for memory emergence: The case of ZnO* [26].

It is also worth noting the many contributions to the author's formation to become a Researcher that this Master Program provided. Through the taken courses, the author have deepened his knowledge on quantum mechanics, electrodynamics, semiconductors devices and computational methods; being all of them very useful skills. But, the most positive gains were, by far, acquired through the research process, in the everyday-life of a researcher, with the challenges and tasks that were presented and with the very frequent and direct contact with researchers and collaborators.

I am grateful to my advisor for proving me the opportunity to see and be part of what it were for me, the first time in my life I have ever done *real* physics research. With him, I have also learned a simple, but also sometimes underestimated concept: that the theory and experiment in physics should always walk together; and fortunately, I had the opportunity to do research following this idea, which were possible just because of the strong collaboration with other researchers.

By working with my advisor and other very capable researchers, I was able to see and learn something about the unique way how each of them proceed in doing research. By means of that I have tried to mimic the best of their methods, adapting it to my style, and

[1] The formalism employed in Chapter 4 is slightly different from the corresponding one of the Theoretical results Chapter. Namely, the $g(V)$ of Chapter 3 has a first order dependence on voltage; while the one employed in Chapter 4 depends on the second order of voltage.

building my personal way of researching (still in development). This, I certainly consider the most valuable skill/experience that I had during this entire process.

5.1 Next steps

The three proposed goals for this Master Course were successfully accomplished. Also, beyond the scope of it, other activities have emerged and they became ongoing research topics to be continued in a PhD. Although some novel extensions of the model have already been done and have also provided enough material to publish two more papers: *"Tuning the conductance topology in solids"* [27] and *"Inadequacy of equivalent circuits in nonlinear systems with inherent memory"* [28]; these topics are still under further investigation; the first, introducing asymmetries to the model and providing the first step to the study of the topology of current-voltage characteristics crossings; and the second one, extending the model to mathematically operate with a infinite number of modes, beyond first or second order, also providing novel interpretation about *equivalent circuits* frequently seen and misunderstood in literature. As there are expectations that innovative results are still to be discovered from them, they were not discussed in this thesis, becoming material for the forthcoming PhD.

Also, the Author has been working in collaboration with his advisor and Professor Ovidiu Lipan, of Richmond University, since the beginning of the Master project, on investigations about memory formation in systems of quantum dots. This is also an ongoing activity that shall continue. Another ongoing activity worth of mentioning is the research on ZnO thin films doped with Nq, that presented a very rich amount of different behaviors under the effect of different atmospheres, and shall become a publishable paper soon.

And to summarize the rich amount of questions or developments that this research provided, the six following questions, still open, can precisely describe and guide what is expected for the forthcoming investigations to be done during a PhD project:

1. Are there universal sufficient conditions for the emergence of memory and can emergent memory device based on different physical principles be mapped onto each other based on symmetry principles?

2. Can we define topological distinguishable classes of emergent memory phenomena and define topological invariants?

3. What are optimal driving configurations of mem-elements and how can one optimize the figure-of-merit based on internal and external control mechanism for different sorts of devices?

4. Can the regularities obtained for continuous models be sustained at the quantum level for single electron devices with memory?

5. Can the memristive response of coupled quantum dots be sustained in both the volatile and the non-volatile limits? How would the memory robustness (loop area) responds to tuning of the input stimuli and intrinsic symmetry constraints?

6. Can a three-phase coupled quantum dot connection be used as a synaptic emulator? If so, which is the optimal driving configuration for such functionality?

Considering the progress done in this thesis and also in the four published papers, we are convinced of being able to answer to these questions to the best of our ability in a forthcoming PhD Thesis.

Bibliography

[1] Rafael Schio Wengenroth Silva, Fabian Hartmann, and Victor Lopez-Richard. The ubiquitous memristive response in solids. *IEEE Transactions on Electron Devices*, 69(9):5351–5356, 2022. Citado 8 vezes nas páginas 8, 15, 16, 17, 31, 34, 36, and 56.

[2] Leon Chua. Memristor-the missing circuit element. *IEEE Transactions on circuit theory*, 18(5):507–519, 1971. Citado na página 15.

[3] Leon O Chua and Sung Mo Kang. Memristive devices and systems. *Proceedings of the IEEE*, 64(2):209–223, 1976. Citado na página 15.

[4] P Maier, Fabian Hartmann, Mariama Rebello Sousa Dias, M Emmerling, C Schneider, LK Castelano, M Kamp, GE Marques, V Lopez-Richard, L Worschech, et al. Mimicking of pulse shape-dependent learning rules with a quantum dot memristor. *Journal of Applied Physics*, 120(13):134503, 2016. Citado na página 15.

[5] Massimiliano Di Ventra and Yuriy V Pershin. The parallel approach. *Nature Physics*, 9(4):200–202, 2013. Citado na página 15.

[6] Sreetosh Goswami, Rajib Pramanick, Abhijeet Patra, Santi Prasad Rath, Martin Foltin, A Ariando, Damien Thompson, T Venkatesan, Sreebrata Goswami, and R Stanley Williams. Decision trees within a molecular memristor. *Nature*, 597(7874):51–56, 2021. Citado na página 15.

[7] S. N. Shevchenko and D. S. Karpov. Thermometry and memcapacitance with a qubit-resonator system. *Phys. Rev. Applied*, 10:014013, Jul 2018. Citado na página 15.

[8] Suhas Kumar, John Paul Strachan, and R Stanley Williams. Chaotic dynamics in nanoscale NbO_2 Mott memristors for analogue computing. *Nature*, 548(7667):318–321, 2017. Citado na página 15.

[9] Suhas Kumar, Xinxin Wang, John Paul Strachan, Yuchao Yang, and Wei D Lu. Dynamical memristors for higher-complexity neuromorphic computing. *Nature Reviews Materials*, 7(7):575–591, 2022. Citado na página 15.

[10] Mario Lanza, Abu Sebastian, Wei D Lu, Manuel Le Gallo, Meng-Fan Chang, Deji Akinwande, Francesco M Puglisi, Husam N Alshareef, Ming Liu, and Juan B Roldan. Memristive technologies for data storage, computation, encryption, and radio-frequency communication. *Science*, 376(6597):eabj9979, 2022. Citado na página 15.

[11] K Miller, F Hartmann, B Leikert, S Kuhn, J Gabel, M Sing, R Claessen, and S Höfling. Room temperature memristive switching in nano-patterned $LaAlO_3/SrTiO_3$ wires with laterally defined gates. *Applied Physics Letters*, 118(15):153502, 2021. Citado na página 15.

[12] Sreetosh Goswami, Adam J. Matula, Santi P. Rath, Svante Hedström, Surajit Saha, Meenakshi Annamalai, Debabrata Sengupta, Abhijeet Patra, Siddhartha Ghosh, Hariom Jani, Soumya Sarkar, Mallikarjuna Rao Motapothula, Christian A. Nijhuis, Jens Martin, Sreebrata Goswami, Victor S. Batista, and T. Venkatesan. Robust resistive memory devices using solution-processable metal-coordinated azo aromatics. *Nature Materials*, 16(12):1216–1224, 2017. Citado na página 15.

[13] Marco Laurenti, Samuele Porro, Candido F. Pirri, Carlo Ricciardi, and Alessandro Chiolerio. Zinc oxide thin films for memristive devices: A review. *Critical Reviews in Solid State and Materials Sciences*, 42(2):153–172, 2017. Citado na página 15.

[14] Christos Giotis, Alex Serb, Spyros Stathopoulos, Loukas Michalas, Ali Khiat, and Themis Prodromakis. Bidirectional volatile signatures of metal–oxide memristors—part i: Characterization. *IEEE Transactions on Electron Devices*, 67(11):5158–5165, 2020. Citado na página 15.

[15] Radu Berdan, Eleni Vasilaki, Ali Khiat, Giacomo LIndiveri, Alexandru Serb, and Themistoklis Prodromakis. Emulating short-term synaptic dynamics with memristive devices. *Scientific Reports*, 6(1):2045–2322, 2016. Citado na página 15.

[16] Lingxiang Hu, Jing Yang, Jingrui Wang, Peihong Cheng, Leon O Chua, and Fei Zhuge. All-optically controlled memristor for optoelectronic neuromorphic computing. *Advanced Functional Materials*, 31(4):2005582, 2021. Citado na página 15.

[17] Lei Wu, Hongxia Liu, Jinfu Lin, and Shulong Wang. Volatile and nonvolatile memory operations implemented in a $Pt/HfO_2/Ti$ memristor. *IEEE Transactions on Electron Devices*, 68(4):1622–1626, 2021. Citado na página 15.

[18] Yuriy V. Pershin and Massimiliano Di Ventra. Memory effects in complex materials and nanoscale systems. *Advances in Physics*, 60(2):145–227, 2011. Citado 2 vezes nas páginas 15 and 16.

[19] C. Giotis, A. Serb, S. Stathopoulos, and T. Prodromakis. Bidirectional volatile signatures of metal-oxide memristors—part ii: Modeling. *IEEE Transactions on Electron Devices*, 67(11):5166–5173, 2020. Citado na página 15.

[20] Sangho Shin, Kyungmin Kim, and Sung-Mo Kang. Compact models for memristors based on charge-flux constitutive relationships. *IEEE Transactions on Computer-*

Aided Design of Integrated Circuits and Systems, 29(4):590–598, 2010. Citado na página 15.

[21] Shiva Asapu and Yuriy V. Pershin. Electromechanical emulator of memristive systems and devices. *IEEE Transactions on Electron Devices*, 62(11):3678–3684, 2015. Citado na página 15.

[22] Fang Yuan, Yue Deng, Yuxia Li, and Guangyi Wang. The amplitude, frequency and parameter space boosting in a memristor–meminductor-based circuit. *Nonlinear Dynamics*, 96:389–405, 2019. Citado na página 15.

[23] G. Alvarado Barrios, J. C. Retamal, E. Solano, and M. Sanz. Analog simulator of integro-differential equations with classical memristors. *Scientific Reports*, 9(1):2045–2322, 2019. Citado na página 15.

[24] Agnes Gubicza, Dávid Zs. Manrique, László Pósa, Colin J. Lambert, György Mihály, Miklós Csontos, and András Halbritter. Asymmetry-induced resistive switching in Ag-Ag_2S-Ag memristors enabling a simplified atomic-scale memory design. *Scientific Reports*, 6(1):2045–2322, 2020. Citado na página 15.

[25] Nasir Ilyas, Dongyang Li, Chunmei Li, Xiangdong Jiang, Yadong Jiang, and Wei Li. Analog switching and artificial synaptic behavior of Ag/SiO_x:Ag/TiO_x/p^{++}-Si memristor device. *Nanoscale Research Letters*, 15(1):1556–276X, 2020. Citado na página 15.

[26] Aline Bastos de Paiva, Rafael Schio Wengenroth Silva, Marcio Peron Franco de Godoy, Luis Miguel Bolaños Vargas, Marcelos Lima Peres, Demetrio A Werner Soares, and Victor Lopez-Richard. Temperature, detriment or advantage for memory emergence: the case of ZnO. *The Journal of Chemical Physics*, 2022 in press. Citado 3 vezes nas páginas 17, 52, and 56.

[27] Victor Lopez-Richard, Rafael Schio Wengenroth Silva, Ovidiu Lipan, and Fabian Hartmann. Tuning the conductance topology in solids. *Journal of Applied Physics*, 133(13), 2023. Citado 2 vezes nas páginas 17 and 57.

[28] Victor Lopez-Richard, RS Silva, Ovidiu Lipan, and Fabian Hartmann. Inadequacy of equivalent circuits in nonlinear systems with inherent memory. *arXiv preprint arXiv:2303.04135*, 2023. Citado 2 vezes nas páginas 18 and 57.

[29] Neil W Ashcroft and N David Mermin. *Solid state physics*. Holt, Rinehart and Winston, 1976. Citado na página 21.

[30] V. L. Bonch-Bruevich and S. G. Kalashnikov. *VI - Effects at contacts*, pages 213–214. Nauka, Moscow, 1977. Citado na página 29.

[31] E. D. Guarin Castro, A. Pfenning, F. Hartmann, G. Knebl, M. Daldin Teodoro, G. E. Marques, S. Höfling, G. Bastard, and V. Lopez-Richard. Optical mapping of nonequilibrium charge carriers. *The Journal of Physical Chemistry C*, 125(27):14741–14750, 2021. Citado na página 29.

[32] Hiroshi Suga, Hiroya Suzuki, Yuma Shinomura, Shota Kashiwabara, Kazuhito Tsukagoshi, Tetsuo Shimizu, and Yasuhisa Naitoh. Highly stable, extremely high-temperature, nonvolatile memory based on resistance switching in polycrystalline pt nanogaps. *Scientific Reports*, 6:34961, 2016. Citado na página 52.